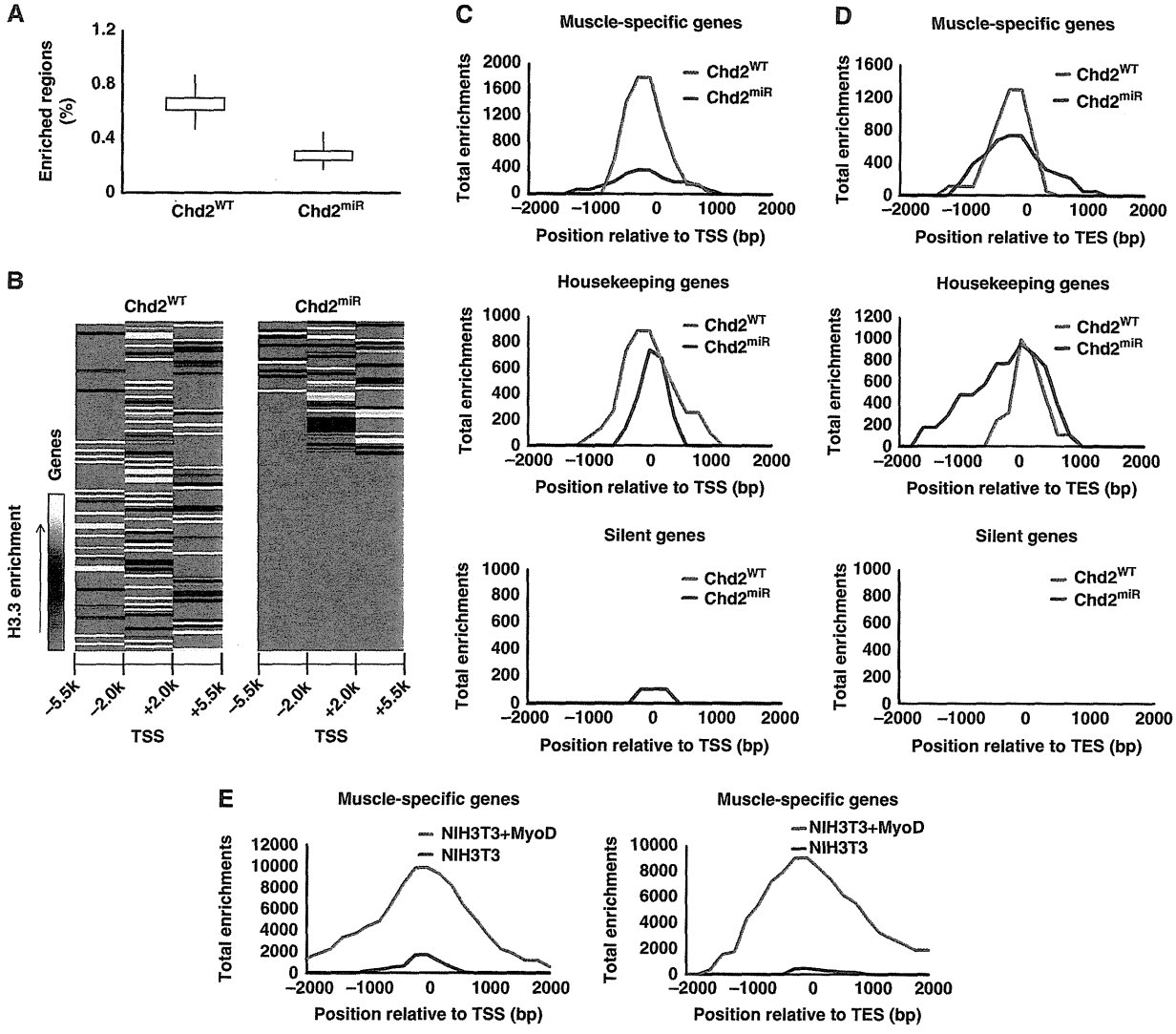

Figure 7 Knockdown of Chd2 decreases the incorporation of H3.3 into the muscle-specific gene loci on a genome-wide level. (**A**) H3.3 deposition in each chromosome is limited. The box plot represents the range of incorporation of H3.3 into each chromosome. (**B**) Chd2 knockdown changes the deposition of H3.3. The heat map represents the enrichment of H3.3 in upregulated genes during myogenic differentiation at the transcriptional start sites (TSS) ± 5.5 kb. The maximum value of H3.3 enrichment is ~10. Each row represents the enrichment pattern of H3.3 along the ± 5.5 kb relative to the TSS. (**C**, **D**) Incorporation of H3.3 at the TSS and TES of muscle-specific, housekeeping, and silent gene loci in undifferentiated C2C12 cells. The H3.3 enrichment Tags from ChIP-Seq data aligned to the TSS and TES were segregated into 200 bp windows. Total enrichments were tallied in muscle-specific, housekeeping and silent genes (Supplementary Dataset 1). (**E**) MyoD-dependent induction of H3.3 incorporation at the TSS (left panel) and TES (right panel) of skeletal muscle gene loci in fibroblast cells ectopically expressing MyoD. Total enrichments were tallied for muscle-specific genes as in (**C**, **D**).

Deposition of H3.3 at differentiation-specific genes contrasts with deposition of H3.3 at the Myod1 locus

Finally, we directly analysed the requirement of H3.3 for myogenic differentiation. siRNA sequences targeting the two H3.3 genes in mouse cells were introduced into C2C12 cells. MHC staining and myotube formation were absent in the cells depleted for H3.3 (Figure 8A). Expression of representative myogenic genes was also compromised upon H3.3 knockdown (Figure 8B). Western blot analysis demonstrated that H3.3 levels, but not H3.1 levels were reduced under both growth and differentiation conditions (Figure 8C).

The data from the H3.3 knockdown experiment is consistent with that from a previous publication that used cells expressing epitope-tagged H3.3 to demonstrate H3.3 incorporation at the locus encoding MyoD (*Myod1*). Specifically, H3.3 incorporation was shown in the proximal regulatory region (PRR) of the *Myod1* locus, 200 bp upstream of the transcription start site, as differentiation proceeded. However, those authors determined that H3.3 incorporation at *Myod1* was dependent on the histone chaperones, HIRA and Asf1a, whereas it was independent of Asf1b and Chd1 (Yang *et al*, 2011). To further investigate, we compared H3.3 incorporation at differentiation-specific genes such as *Acta1* and *Myog* with *Myod1* PRR in undifferentiated cells. Consistent with the results presented above, knockdown of Chd2 prevented H3.3 incorporation at *Acta1* and *Myog* (Figure 8D). Chd2 knockdown had no effect on H3.3 incorporation at the *Myod1* sequence or at the housekeeping genes. Interestingly, H3.3 knockdown prevented H3.3

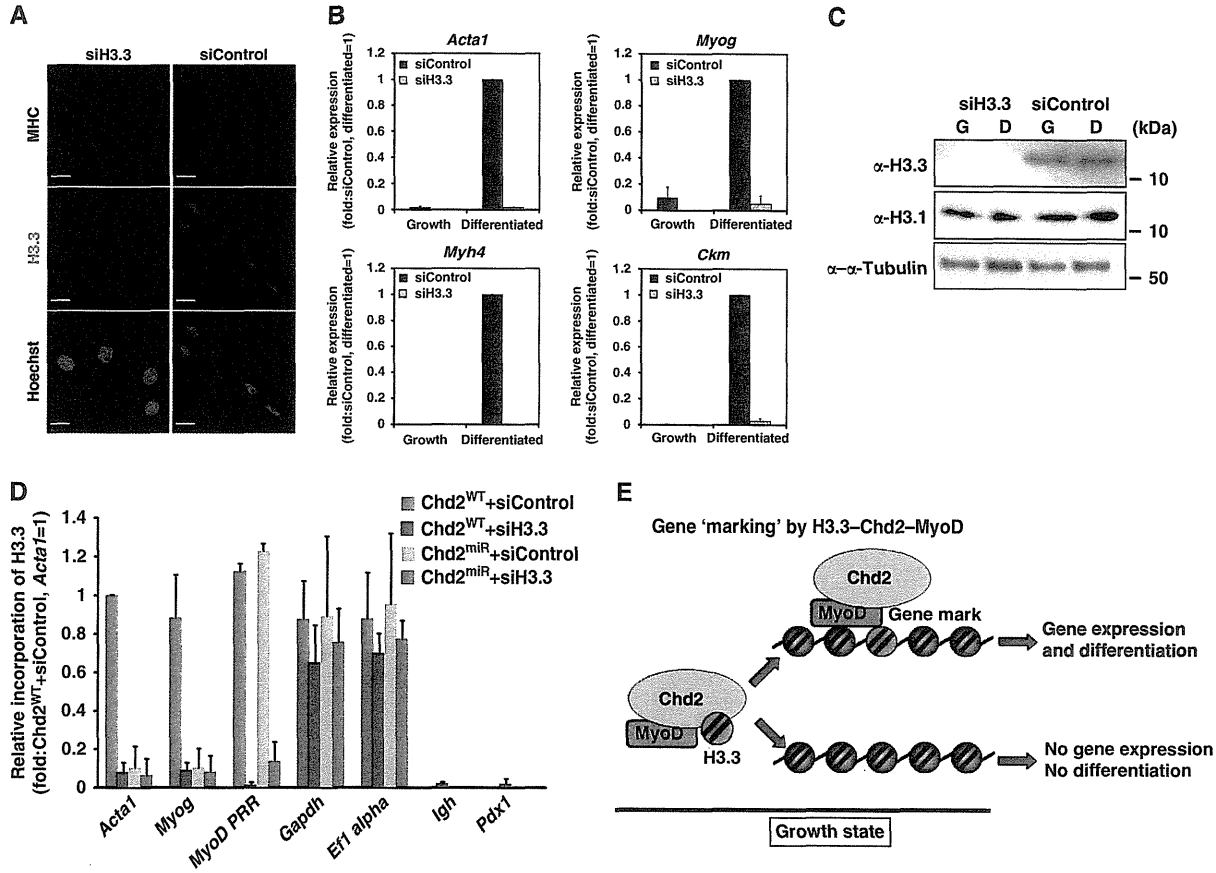

Figure 8 H3.3 is required for myogenic differentiation. (**A**) The expression of myosin heavy chain (MHC; red) and myotube formation was not induced in C2C12 cells when H3.3 expression was suppressed by siRNAs targeting *H3f3a* and *H3f3b*. Scale bars = 5 μm. (**B**) The transcription of skeletal muscle marker genes was suppressed in C2C12 cells expressing siRNAs targeting *H3f3a* and *H3f3b*. mRNA levels were analysed by Q-PCR; data represent the average of three independent experiments ± s.d. (**C**) Western blot evaluating H3.3 protein knockdown and the expression of the other indicated proteins. (**D**) siRNA-mediated H3.3 knockdown inhibits H3.3 recruitment onto *Acta1*, *Myog* and *Myod1*, while in Chd2 knockdown cells, H3.3 incorporation is not decreased at *Myod1*. ChIP assays were performed as in Figure 6. (**E**) Schematic representation of the 'marking' of myogenic genes by Chd2 prior to myogenesis. Chd2 coordinates with MyoD to direct H3.3 to differentiation-dependent, skeletal muscle-specific gene loci during the growth state. Incorporation of H3.3 marks myogenic loci for expression following the initiation of the differentiation process.

incorporation at the myogenic sequences tested but did not affect H3.3 incorporation at the housekeeping genes (Figure 8D). Though the reasons remain to be explored, this result suggests that under conditions of H3.3 depletion, incorporation of the remaining H3.3 is non-random. Regardless, these data, coupled with the earlier report (Yang *et al*, 2011) clearly demonstrate that the mechanisms controlling deposition of H3.3 at the *Myod1* locus differ from those controlling H3.3 incorporation at downstream myogenic genes activated upon differentiation.

In summary, our directed and genome-wide profiling of H3.3 incorporation provides a mechanism accounting for the inhibition of myogenesis caused by knockdown of Chd2. A schematic drawing outlining Chd2-dependent deposition of H3.3 to mark differentiation-specific genes prior to the onset of differentiation and differentiation-specific gene expression is presented in Figure 8E.

Discussion

We showed that Chd2-mediated H3.3 deposition helps determine the gene expression programme for skeletal muscle differentiation. Our results suggest that Chd2 participates in selecting whether a gene will be expressed during muscle differentiation via its localization to myogenic gene loci in the undifferentiated state. The selected gene is then marked for expression by Chd2-dependent incorporation of H3.3 into the gene locus. The presence of the H3.3 variant in chromatin is associated with histone modifications that generally signal transcriptionally poised or transcriptionally competent chromatin (Wirbelauer *et al*, 2005; Hake *et al*, 2006; Goldberg *et al*, 2010) and has been proposed to be associated with epigenetic memory (Hake and Allis, 2006; Ng and Gurdon, 2008). Thus, the deposition of H3.3 at myogenic genes in myoblast cells represents a mechanism by which differentiation-specific genes can be marked for activation once differentiation signalling induces the onset of myogenesis.

The enzymatic activities of Chd2 are not well characterized. Analysis of Chd2 mutant mice indicated that Chd2 plays a critical role in development and tumour suppression (Marfella *et al*, 2006; Nagarajan *et al*, 2009). Moreover, Chd2 appears to be ubiquitously expressed, though highly enriched in muscle tissues (Marfella *et al*, 2006). The closely

related Chd1 enzyme, however, has been shown to incorporate H3.3 into nucleosomes in a Hira-independent manner (Konev *et al*, 2007). CHD1 also binds to the K4me3 mark associated with the activation of gene expression (Sims *et al*, 2005), and Chd1 is essential for maintaining pluripotency in ES cells (Gaspar-Maia *et al*, 2009). Despite the structural similarity of the Chd1 and Chd2 proteins, they do not appear to be redundant, because the data presented here indicates that in undifferentiated and differentiated cells, Chd2, but not Chd1, interacts with MyoD and that Chd2 associates with H3.3 with greater frequency than does Chd1. The functional relationship between these two structurally related proteins remains to be determined.

The ChIP-Seq analysis of H3.3 using next-generation sequencing represents the first analysis of endogenous H3.3 incorporation into chromatin in any genome. The data indicate that H3.3 incorporation is extremely limited across the myoblast genome, and is concentrated at both the TSS and the TES of transcribed genes. The localization of H3.3 is not surprising; earlier studies of epitope-tagged H3.3 also revealed that it localizes near the TSS and TES of actively transcribed genes (Jin *et al*, 2009). The significance of localization to TES of active genes is not presently understood. Unexpectedly, the data indicate that knockdown of Chd2 not only reduced H3.3 incorporation at some genes but also showed enhanced incorporation at other genes. This might indicate that Chd2 both positively and negatively regulates incorporation of H3.3 across the genome. Alternatively, or in addition, other proteins that can modulate H3.3 incorporation (Yang *et al*, 2011) may have altered activities or altered targets upon misregulation of Chd2 levels.

We found that Chd2 specifically associates with MyoD in the undifferentiated state by three distinct methods: co-IP, co-localization by immunofluorescence, and PLA. Although we did not perform the co-IP experiment in differentiated cells, we did utilize the co-immunofluorescence and PLA assays to demonstrate that the MyoD–Chd2 interaction remains during differentiation. The MyoD-related protein Myf5 can compensate for the function of MyoD; however, we were unable to assess whether Myf5 could bind Chd2 or to Chd2 target genes as we were unable to identify an antibody that could reliably immunoprecipitate Myf5. While we cannot exclude the possibility that Myf5 also contributes to Chd2 function, the data presented suggest that MyoD is required for Chd2 binding to and for Chd2-dependent deposition of H3.3 at myogenic sequences.

Though gene-specific evidence for MyoD binding to target genes before differentiation is limited (Mal and Harter, 2003), a genomic analysis of MyoD binding in C2C12 myoblasts indicates that MyoD is bound widely throughout the genome, including at most myogenic genes (Cao *et al*, 2010). These findings provide a mechanism to explain the selective targeting of Chd2 to myogenic genes in the undifferentiated state. Once marked by incorporation of H3.3, the gene is ready to be transcribed upon differentiation signalling, which results in numerous molecular changes at myogenic regulatory sequences and throughout these loci (Tapscott, 2005; Keren *et al*, 2006).

The data presented here demonstrate that differentiation-specific myogenic genes are marked by incorporation of the H3.3 histone variant in a manner dependent upon MyoD and the Chd2 enzyme. This contrasts with deposition of H3.3 at the *Myod1* locus (Yang *et al*, 2011), which is independent of Chd2 but is consistent with the idea that MyoD itself is expressed prior to differentiation. These marks occur prior to the onset of differentiation and gene expression, and the absence of these marks precludes myogenic gene expression. Thus, the MyoD–Chd2–H3.3 axis provides a novel mechanism for potentiating the expression of differentiation-specific genes upon subsequent differentiation signalling.

Materials and methods

Cells

C2C12 cells were cultured in Dulbecco's modified Eagle's medium (DMEM) supplemented with 20% fetal bovine serum. Cells examined under growth conditions were harvested at 60–70% confluency. Differentiated samples were transferred to DMEM containing 2% horse serum upon reaching confluence and harvested 48 h later. The NIH3T3-derived cell (B22) line was infected with retrovirus expressing MyoD as described previously (de la Serna *et al*, 2001).

miRNA expression constructs

The oligonucleotides used for expression of *Chd2* and for the negative control (*lacZ*) miRNAs are described in Supplementary Table SI. Annealed oligonucleotides were ligated into pT2A–CAG/EGFP–NLS, which contains TolII transposon elements and EGFP–NLS cDNA located upstream of the miRNA sequence and which was modified from pT2AL200R150G (Kawakami and Noda, 2004; Kawakami *et al*, 2004; Urasaki *et al*, 2006).

Plasmid transfection and cell line selection

The pT2A–CAG/EGFP–NLS–miRNA transfection was performed using Gene Juice transfection 2 reagent (Novagen). C2C12 cells at 20–30% confluence were transfected with a miRNA expression vector (6 μg plasmid DNA per 100-mm plate), pCAGGS-TP coding transposase (provided by Dr Kawakami), and pT2A–CAG/puromycin and incubated for 24 h. To create cell lines stably expressing miRNAs targeting *Chd2*, we transfected cells with four distinct candidate miRNAs (Supplementary Table SI). To create a control line, cells were transfected with a miRNA against *lacZ*. Transfected cells were cultured for 7 days in the presence of 2 μg/ml puromycin. From the four pools of transfectants, we selected the two ($Chd2^{miR3139}$, $Chd2^{miR5111}$) that showed the greatest suppression of Chd2 expression. We then created single cell clones from each pool, as well as from the control ($Chd2^{WT}$) pool, by dilution such that one cell was plated per every 24 wells of a 96-well plate. Four monoclonal lines were chosen from each of the original pools based on the extent of the Chd2 knockdown. All four $Chd2^{miR3139}$ clones and all four $Chd2^{miR5111}$clones showed suppression of Chd2 expression, inhibition of myogenic gene expression, and inhibition of myotube formation when differentiation was induced. All four of the $Chd2^{WT}$ clones showed no change in Chd2 expression compared with parental C2C12 cells and showed no change in myogenic expression or myotube formation when induced to differentiate. One of each clone for $Chd2^{miR3139}$, $Chd2^{miR5111}$, and $Chd2^{WT}$ was chosen for further study. All experiments were completed with cell lines that were passaged 10 times or less.

Rescue experiments

Each competitive mRNA fragment (*Chd2*-3011-3283, *Chd2*-5004-5177) was ligated downstream of the mKO1–NLS mRNA in the pT2A/CAG expression vector. Stable transfection was performed to introduce both the *Chd2*-targeting miRNA and the competitive mRNA fragment as indicated.

Each cDNA (*Chd2* full-length or *Chd2*(Δ281–512 aa)) was ligated downstream of the mKO2 mRNA in the Bidirectional Tet Expression Vector pTETmKO2 (Clontech Tet-On system and (Sakaue-Sawano *et al*, 2008)). Stable transfection was performed to introduce both the *Chd2*-targeting miRNA and the indicated *Chd2* cDNA.

Monoclonal antibodies

The Chd1, Chd2, MyoD, Brm, and Brg1 rat monoclonal antibodies were described (Ohkawa *et al*, 2009; Okada *et al*, 2009; Harada *et al*, 2010a, b; Yoshimura *et al*, 2010). The H3.3 and H3.1 antigens were

synthesized based on their specific sequences, H3.3: CATKAARKSA PSTGGVKKPH (AA 21–39) and H3.1: CATKAARKSAPATGGVKKPH (AA 21–39 aa) (Sigma-Aldrich). The N-terminal cysteine residue allowed coupling to maleimide-activated keyhole limpet haemocyanin (Thermo Scientific), a carrier protein. The coupling reaction followed the instructions provided the supplier. Rat (H3.3) or mouse (H3.1) monoclonal antibodies were generated based on the lymph node method established by Sado *et al* (1995)(Kishiro *et al*, 1995). In all, 200 μg H3.3 or H3.1 peptide was used as antigen. Hybridoma cells were cloned in HAT selection medium (hybridoma SFM medium (Invitrogen); 10% fetal bovine serum; 10% BM-Condimed H1 (Roche); 100 μM hypoxanthine; 0.4 μM aminopterin; 1.6 μM thymidine) and were screened 7 days post-fusion using an enzyme-linked immunoadsorbent assay (ELISA) against each antigen. H3.3-positive clone specificity was confirmed by checking cross-reactivity for the H3.1 peptide and H3.1-positive clone specificity was confirmed by checking cross-reactivity for the H3.3 peptide. Positive clones were subcloned and rescreened by ELISA. Concentrated antibody preparations were made from clones 4H2D7 (for H3.3) and 1D4F2 (for H3.1) that were cultured at high density using a miniPERM bioreactor (Vivascience).

ELISA

BSA-conjugated H3.3 or H3.1 peptide (5 μg/ml) was diluted from 1:100 to 1:100 000 in 10 mM sodium phosphate pH 7.0 and then adsorbed on Costar Serocluster 96-Well 'U' Bottom Plates (Corning) at 4°C for 12–24 h. The plates were subsequently blocked with 1% BSA in PBS to prevent non-specific associations. Hybridoma supernatants were applied for 1 h at room temperature followed by three PBS washes and then 30 min incubation at room temperature with alkaline phosphatise-conjugated anti-rat or anti-mouse IgG antibody (Sigma) diluted to 1:10 000. Immunoreactivity was identified by a pNPP phosphatase substrate system (KPL) after washing with TBS-T three times.

Immunoprecipitation, immunoblotting, and ICC

IP, western blot analysis, and ICC were performed as described (Harada *et al*, 2010b). For IP, cleared lysates were rocked with 10 μl of rabbit antisera against MyoD (de la Serna *et al*, 2005) or 100 μl supernatant of monoclonal antibody against Chd2 (ascites, 8H3) for 12 h. For immunoblotting, primary antibodies used included rabbit anti-MyoD (C-20, Santa Cruz Biotechnology, 1:1000; Figure 1A only), anti-cyclin A (C-19, Santa Cruz Biotechnology, 1:1000), anti-cyclin E (M-20, Santa Cruz Biotechnology, 1:1000), anti-α-tubulin (Cell Signaling, 1:2000), anti-H3 (Cell Signaling, 1:1000), mouse anti-GFP (GF200, Nacalai Tesque, 1:500), rat anti-Chd2 (8H3, hybridoma supernatant, 1:100), anti-H3.3 (hybridoma supernatant, 1:1000), anti-H3.1 (hybridoma supernatant, 1:1000), anti-MyoD (hybridoma supernatant, 1:100), and anti-Chd1 (hybridoma supernatant, 1:1000). Secondary antibodies were horseradish peroxidase-conjugated anti-rabbit, anti-mouse, or anti-rat IgG antibodies (1:5000; GE Healthcare). For ICC, 1% paraformaldehyde was used for fixation. Primary antibodies included rat monoclonal anti-Chd2 (8H3, hybridoma supernatant, 1:50), anti-Chd1 (2F11, hybridoma supernatant, 1:100), anti-H3.3 (4H2D7, hybridoma supernatant, 1:2), rabbit anti-myosin heavy chain (Calbiochem, 1:100), anti-Myogenin (M-225, Santa Cruz Biotechnology, 1:500), or anti-MyoD (C-20, Santa Cruz Biotechnology, 1:200), mouse anti-H3K4me3 (gifted from Dr H Kimura, 1:1000) (Kimura *et al*, 2008), anti-H3K9me2 (gifted from Dr H Kimura, 1:1000) (Hayashi-Takanaka *et al*, 2011). Images were visualized using a confocal microscope (LSM510; Carl Zeiss). Co-localization was evaluated by ImageJ (NCBI). Co-localization frequency was analysed as described previously (vanSteensel *et al*, 1996), except that the cross-correlation function was calculated by rotating the red image (labelling Alexa-588) over an angle $x°$ in the x orientation with respect to the green image (labelling Alexa-488) such as $-90 = x = 90$. A negative value of x indicates that the red image was rotated counterclockwise, and a positive value indicates a clockwise rotation. Pearson's correlation coefficient (γ_P) was calculated for each value of x and plotted against x to obtain the cross-correlation function (vanSteensel *et al*, 1996).

Proximity ligation assay

Proximity ligation was performed using a Duolink assay kit II (OlinkBiosciences) according to the protocol provided by manufacturer, except that the oligonucleotide-conjugated anti-rabbit probe was used at 1:20 and the anti-rat probe conjugated by probemaker was used at 1:40. Finally, the coverslips were again mounted with Duolink Mounting Medium contained Bisbenzimide H33342 Fluorochrome Trihydrochloride (Hoechst). All images were taken with an epifluorescence microscope (BX51; Olympus) with ×40 objective and analysed with NIH ImageJ software. Three images were taken from each sample. Antibodies used included the affinity purified rabbit anti-MyoD (de la Serna *et al*, 2005) and rat monoclonals against Brg1 and Chd2 (Ohkawa *et al*, 2009; Harada *et al*, 2010b) for Figure 1D and 1E. In Figure 5, the rat H3.3 and mouse H3.1 monoclonals described above were used with affinity purified rabbit antibody generated against the Chd2 antigen described previously (Harada *et al*, 2010b).

Quantitative RT–PCR

Total RNA was isolated and reversed-transcribed with Takara Prime Script Reverse Transcriptase and an oligo dT primer as described (Valdez *et al*, 2000). Q-PCR was performed using TaKaRa SYBR Premix Dimer Eraser and primers listed in Supplementary Table SII. Q-PCR data are presented as mean ± s.d. of three independent experiments.

Fluorescence-activated cell sorting (FACS)

FACS analysis of propidium iodide-stained cells was performed as described (Dacwag *et al*, 2007).

siRNA-mediated knockdown of MyoD, Chd2, and H3.3

Knockdown of MyoD, Chd2, H3.3 was performed by transfection of the C2C12 cells with siRNA duplex oligos (Kumar *et al*, 2003; Yang *et al*, 2011) using Lipofectamine RNAiMAX (Invitrogen) according to the manufacturer's protocol. Control RNAi (Mission_Negative control SIC-001; proprietary sequence), MyoD–RNAi: (5′-GGCCUG UCAAGUCUAUGUC-3′ and 5′-GGCAUAGACUUGACAGGCC-3′), H3f3a–RNAi: (5′-GAGAAAUUG CUC AGGACU UTT-3′ and 5′-AAG UCCUGAGCAAUUUCUCTT-3′), H3f3b–RNAi: (5′-CAGAGAUUG GUG AGGGAGA TT-3′ and 5′-UCUCCCUCACCAAUCUCUGTT-3′) were synthesized by Sigma. Chd2–RNAi: (5′-AAAUCCUGCUGGUGAUA AUUCUGGG-3′ and 5′-CCCAGAAUUAUCACCAGCAGGAUUU-3′) were synthesized by Invitrogen.

Chromatin immunoprecipitation

ChIP assays were performed by modifying the Upstate Biotechnology protocol as described previously (Dacwag *et al*, 2007) utilizing the rat monoclonal antibodies against Chd2 (8H3, ascites, 20 μl) and H3.3 (4H2D7, ascites, 20 μl). Relative recruitment or incorporation was defined as the ratio of amplification of the PCR product relative to 1% of input genomic DNA. Quantification represents the mean of three independent experiments ± s.d. ChIP experiments using IgG were performed as controls (Supplementary Figure S8). The primers used to amplify the promoter regions are listed in Supplementary Table SIII. Re-ChIP assays were performed as described previously (Ohkawa *et al*, 2006).

ChIP-seq and data analysis

Sample preparation was performed as described above except cells were not fixed. The ChIP library was prepared with the Illumina protocol and sequencing analysis was performed using the Genome Analyser GAIIx (Illumina KK). The base-called sequences were obtained using SCS2.7 from ChIP-seq image data. The sequence tags for H3.3 and Input were aligned to the mouse genome (mm9) using ELAND v2, BWA (Li and Durbin, 2009), and Bowtie (Langmead *et al*, 2009) software. We adapted the alignment data of Bowtie so that the alignment efficiency was optimized. Unique tag numbers are listed in Supplementary Table SIV. Peak detection and identification of binding sites of H3.3 were obtained by correcting from Input DNA using MACS (Zhang *et al*, 2008) with default parameters except bw = 300 based on the fragmented size of the ChIP sample. The calculated FDR was ⩽0.1%. The box plot of H3.3-enriched regions was obtained giving the sum total of the enrichment area (bp) of H3.3, found in MACS, of each chromosome divided by the length (bp) of each chromosome. The heat map was generated from H3.3 enrichment of the genes that were upregulated after induction of skeletal muscle differentiation (Supplementary Dataset 1), based on the microarray analysis in C2C12 cells (Tomczak *et al*, 2004). The maximum value of H3.3 enrichment is ~10. Each row represents the enrichment pattern of H3.3 along the

±5.5 kb relative to the TSS. The total enrichments of TSS/TES ±2 kb obtained by the H3.3 enrichment Tags aligned at TSS/TES that were segregated into 200 bp windows were tallied for skeletal muscle-specific genes, housekeeping genes and silent genes in C2C12 cells, based on published microarray analyses in C2C12 cells, NIH3T3 cells, and RAW264.7 cells (Tomczak *et al*, 2004; Berenjeno *et al*, 2007; Covert *et al*, 2009). Microarray data were obtained from NCBI GEO GSM137347(NIH3T3), GSE989(C2C12), GSM197840(RAW264.7). All defined gene lists are shown in Supplementary Dataset 1. Reference gene annotation was determined using the UCSC genome browser (http://genome.ucsc.edu).

Accession numbers

ChIP-seq data were deposited with accession codes DRA000164, DRA000165, DRA000166, DRA000218, and DRA000219 (DNA Data Bank of Japan).

Supplementary data

Supplementary data are available at *The EMBO Journal* Online (http://www.embojournal.org).

Acknowledgements

We thank Dr K Kawakami for providing plasmids; Dr Kimura for providing monoclonal antibodies; Dr K Maeshima for advice; and Mr Maehara, Ms Ichinose, Itoh, Koga, Miharu, and Onishi for technical support. This work was supported in part by grants from the Ministry of Education, Culture, Sports, Science, and Technology of Japan, the Kaibara Morikazu Medical Science Promotion Foundation, and by NIH Grant GM56244.

Author contributions: AH designed and performed the experiments and wrote the manuscript. SO contributed ideas and interpreted the results. DK performed the experiments related to miRNA expression. JO performed the immunoprecipitation experiments. TY, SY, and T Tachibana established and characterised rat monoclonal antibodies. H Kumamaru, HS, and T Tsubota interpreted the results. H Kurumizaka provided recombinant H3.1 and H3.3 proteins. KA interpreted the results. ANI contributed ideas, interpreted the results, and wrote the manuscript. YO designed the project, designed experiments, contributed ideas, interpreted results, and wrote the manuscript.

Conflict of interest

The authors declare that they have no conflict of interest.

References

Ahmad K, Henikoff S (2002) The histone variant H3.3 marks active chromatin by replication-independent nucleosome assembly. *Mol Cell* **9:** 1191–1200

Berenjeno IM, Nunez F, Bustelo XR (2007) Transcriptomal profiling of the cellular transformation induced by Rho subfamily GTPases. *Oncogene* **26:** 4295–4305

Cao Y, Yao Z, Sarkar D, Lawrence M, Sanchez GJ, Parker MH, MacQuarrie KL, Davison J, Morgan MT, Ruzzo WL, Gentleman RC, Tapscott SJ (2010) Genome-wide MyoD binding in skeletal muscle cells: a potential for broad cellular reprogramming. *Dev Cell* **18:** 662–674

Covert J, Mathison AJ, Eskra L, Banai M, Splitter G (2009) Brucella melitensis, B. neotomae and B. ovis elicit common and distinctive macrophage defense transcriptional responses. *Exp Biol Med (Maywood)* **234:** 1450–1467

Dacwag CS, Ohkawa Y, Pal S, Sif S, Imbalzano AN (2007) The protein arginine methyltransferase Prmt5 is required for myogenesis because it facilitates ATP-dependent chromatin remodeling. *Mol Cell Biol* **27:** 384–394

Davis RL, Weintraub H, Lassar AB (1987) Expression of a single transfected CDNA converts fibroblasts to myoblasts. *Cell* **51:** 987–1000

de la Serna IL, Carlson KA, Imbalzano AN (2001) Mammalian SWI/SNF complexes promote MyoD-mediated muscle differentiation. *Nature Genet* **27:** 187–190

de la Serna IL, Ohkawa Y, Berkes CA, Bergstrom DA, Dacwag CS, Tapscott SJ, Imbalzano AN (2005) MyoD targets chromatin remodeling complexes to the myogenin locus prior to forming a stable DNA-bound complex. *Mol Cell Biol* **25:** 3997–4009

Garcia BA, Pesavento JJ, Mizzen CA, Kelleher NL (2007) Pervasive combinatorial modification of histone H3 in human cells. *Nat Methods* **4:** 487–489

Gaspar-Maia A, Alajem A, Polesso F, Sridharan R, Mason MJ, Heidersbach A, Ramalho-Santos J, McManus MT, Plath K, Meshorer E, Ramalho-Santos M (2009) Chd1 regulates open chromatin and pluripotency of embryonic stem cells. *Nature* **460:** 863–U897

Goldberg AD, Banaszynski LA, Noh KM, Lewis PW, Elsaesser SJ, Stadler S, Dewell S, Law M, Guo XY, Li X, Wen DC, Chapgier A, DeKelver RC, Miller JC, Lee YL, Boydston EA, Holmes MC, Gregory PD, Greally JM, Rafii S *et al* (2010) Distinct factors control histone variant H3.3 localization at specific genomic regions. *Cell* **140:** 678–691

Hake SB, Allis CD (2006) Histone H3 variants and their potential role in indexing mammalian genomes: the 'H3 barcode hypothesis'. *Proc Natl Acad Sci USA* **103:** 6428–6435

Hake SB, Garcia BA, Duncan EM, Kauer M, Dellaire G, Shabanowitz J, Bazett-Jones DP, Allis CD, Hunt DF (2006) Expression patterns and post-translational modifications associated with mammalian histone H3 variants. *J Biol Chem* **281:** 559–568

Harada A, Ohkawa Y, Ao S, Odawara J, Okada S, Azuma M, Nishiyama Y, Nakamura M, Tachibana T (2010a) Rat monoclonal antibody specific for MyoD. *Hybridoma (Larchmt)* **29:** 255–258

Harada A, Yoshimura S, Odawara J, Azuma M, Okada S, Nakamura M, Tachibana T, Ohkawa Y (2010b) Generation of a rat monoclonal antibody specific for CHD2. *Hybridoma (Larchmt)* **29:** 173–177

Hayashi-Takanaka Y, Yamagata K, Wakayama T, Stasevich TJ, Kainuma T, Tsurimoto T, Tachibana M, Shinkai Y, Kurumizaka H, Nozaki N, Kimura H (2011) Tracking epigenetic histone modifications in single cells using Fab-based live endogenous modification labeling. *Nucleic Acids Res* **39:** 6475–6488

Jin CY, Zang CZ, Wei G, Cui KR, Peng WQ, Zhao KJ, Felsenfeld G (2009) H3.3/H2A.Z double variant-containing nucleosomes mark 'nucleosome-free regions' of active promoters and other regulatory regions. *Nat Genet* **41:** 941–U112

Karasawa S, Araki T, Nagai T, Mizuno H, Miyawaki A (2004) Cyan-emitting and orange-emitting fluorescent proteins as a donor/acceptor pair for fluorescence resonance energy transfer. *Biochem J* **381:** 307–312

Kawakami K, Noda T (2004) Transposition of the Tol2 element, an Ac-like element from the Japanese medaka fish Oryzias latipes, in mouse embryonic stem cells. *Genetics* **166:** 895–899

Kawakami K, Takeda H, Kawakami N, Kobayashi M, Matsuda N, Mishina M (2004) A transposon-mediated gene trap approach identifies developmentally regulated genes in zebrafish. *Dev Cell* **7:** 133–144

Keren A, Tamir Y, Bengal E (2006) The p38 MAPK signaling pathway: A major regulator of skeletal muscle development. *Mol Cell Endocrinol* **252:** 224–230

Kimura H, Hayashi-Takanaka Y, Goto Y, Takizawa N, Nozaki N (2008) The organization of histone H3 modifications as revealed by a panel of specific monoclonal antibodies. *Cell Struct Function* **33:** 61–73

Kishiro Y, Kagawa M, Naito I, Sado Y (1995) A novel method of preparing rat-monoclonal antibody-producing hybridomas by using rat medial iliac lymph-node cells. *Cell Struct Function* **20:** 151–156

Konev AY, Tribus M, Park SY, Podhraski V, Lim CY, Emelyanov AV, Vershilova E, Pirrotta V, Kadonaga JT, Lusser A, Fyodorov DV (2007) CHD1 motor protein is required for deposition of histone variant h3.3 into chromatin *in vivo*. *Science* **317:** 1087–1090

Kouskouti A, Talianidis I (2005) Histone modifications defining active genes persist after transcriptional and mitotic inactivation. *EMBO J* **24:** 347–357

Kumar R, Conklin DS, Mittal V (2003) High-throughput selection of effective RNAi probes for gene silencing. *Genome Res* **13:** 2333–2340

Langmead B, Trapnell C, Pop M, Salzberg SL (2009) Ultrafast and memory-efficient alignment of short DNA sequences to the human genome. *Genome Biol* **10:** R25

Li H, Durbin R (2009) Fast and accurate short read alignment with Burrows-Wheeler transform. *Bioinformatics* **25:** 1754–1760

Mal A, Harter ML (2003) MyoD is functionally linked to the silencing of a muscle-specific regulatory gene prior to skeletal myogenesis. *Proc Natl Acad Sci USA* **100:** 1735–1739

Marfella CGA, Ohkawa Y, Coles AH, Garlick DS, Jones SN, Imbalzano AN (2006) Mutation of the SNF2 family member Chd2 affects mouse development and survival. *J Cell Physiol* **209:** 162–171

Meshorer E, Yellajoshula D, George E, Scambler PJ, Brown DT, Mistell T (2006) Hyperdynamic plasticity in pluripotent embryonic of chromatin proteins stem cells. *Dev Cell* **10:** 105–116

Nagarajan P, Onami TM, Rajagopalan S, Kania S, Donnell R, Venkatachalam S (2009) Role of chromodomain helicase DNA-binding protein 2 in DNA damage response signaling and tumorigenesis. *Oncogene* **28:** 1053–1062

Ng RK, Gurdon JB (2008) Epigenetic memory of an active gene state depends on histone H3.3 incorporation into chromatin in the absence of transcription. *Nat Cell Biol* **10:** 102–U183

Ohkawa Y, Harada A, Nakamura M, Yoshimura S, Tachibana T (2009) Production of a rat monoclonal antibody against Brg1. *Hybridoma (Larchmt)* **28:** 463–466

Ohkawa Y, Marfella CGA, Imbalzano AN (2006) Skeletal muscle specification by myogenin and Mef2D via the SWI/SNF ATPase Brg1. *EMBO J* **25:** 490–501

Okada S, Harada A, Saiwai H, Nakamura M, Ohkawa Y (2009) Generation of a Rat Monoclonal Antibody Specific for Brm. *Hybridoma* **28:** 455–458

Okano M, Bell DW, Haber DA, Li E (1999) DNA methyltransferases Dnmt3a and Dnmt3b are essential for *de novo* methylation and mammalian development. *Cell* **99:** 247–257

Pray-Grant MG, Daniel JA, Schieltz D, Yates JR, Grant PA (2005) Chd1 chromodomain links histone H3 methylation with SAGA- and SLIK-dependent acetylation. *Nature* **433:** 434–438

Ray-Gallet D, Quivy JP, Scamps C, Martini EMD, Lipinski M, Almouzni G (2002) HIRA is critical for a nucleosome assembly pathway independent of DNA synthesis. *Mol Cell* **9:** 1091–1100

Sado Y, Kagawa M, Kishiro Y, Sugihara K, Naito I, Seyer JM, Sugimoto M, Oohashi T, Ninomiya Y (1995) Establishment by the rat lymph-node method of epitope-defined monoclonal-antibodies recognizing the 6 different alpha-chains of human Type-Iv collagen. *Histochem Cell Biol* **104:** 267–275

Sakaue-Sawano A, Kurokawa H, Morimura T, Hanyu A, Hama H, Osawa H, Kashiwagi S, Fukami K, Miyata T, Miyoshi H, Imamura T, Ogawa M, Masai H, Miyawaki A (2008) Visualizing spatiotemporal dynamics of multicellular cell-cycle progression. *Cell* **132:** 487–498

Simone C, Forcales SV, Hill DA, Imbalzano AN, Latella L, Puri PL (2004) p38 pathway targets SWI-SNF chromatin-remodeling complex to muscle-specific loci. *Nat Genet* **36:** 738–743

Sims RJ, Chen CF, Santos-Rosa H, Kouzarides T, Patel SS, Reinberg D (2005) Human but not yeast CHD1 binds directly and selectively to histone H3 methylated at lysine 4 via its tandem chromodomains. *J Biol Chem* **280:** 41789–41792

Takahashi K, Yamanaka S (2006) Induction of pluripotent stem cells from mouse embryonic and adult fibroblast cultures by defined factors. *Cell* **126:** 663–676

Tapscott SJ (2005) The circuitry of a master switch: Myod and the regulation of skeletal muscle gene transcription. *Development* **132:** 2685–2695

Tomczak KK, Marinescu VD, Ramoni MF, Sanoudou D, Montanaro F, Han M, Kunkel LM, Kohane IS, Beggs AH (2004) Expression profiling and identification of novel genes involved in myogenic differentiation. *FASEB J* **18:** 403–405

Tontonoz P, Hu ED, Spiegelman BM (1994) Stimulation of adipogenesis in fibroblasts by Ppar-Gamma-2, a lipid-activated transcription factor. *Cell* **79:** 1147–1156

Urasaki A, Morvan G, Kawakami K (2006) Functional dissection of the Tol2 transposable element identified the minimal cis-sequence and a highly repetitive sequence in the subterminal region essential for transposition. *Genetics* **174:** 639–649

Valdez MR, Richardson JA, Klein WH, Olson EN (2000) Failure of Myf5 to support myogenic differentiation without myogenin, MyoD, and MRF4. *Dev Biol* **219:** 287–298

vanSteensel B, vanBinnendijk EP, Hornsby CD, vanderVoort HTM, Krozowski ZS, deKloet ER, vanDriel R (1996) Partial colocalization of glucocorticoid and mineralocorticoid receptors in discrete compartments in nuclei of rat hippocampus neurons. *J Cell Sci* **109:** 787–792

Wirbelauer C, Bell O, Schubeler D (2005) Variant histone H3.3 is deposited at sites of nucleosomal displacement throughout transcribed genes while active histone modifications show a promoter-proximal bias. *Genes Dev* **19:** 1761–1766

Yang JH, Song Y, Seol JH, Park JY, Yang YJ, Han JW, Youn HD, Cho EJ (2011) Myogenic transcriptional activation of MyoD mediated by replication-independent histone deposition. *Proc Natl Acad Sci USA* **108:** 85–90

Yoshimura S, Harada A, Odawara J, Azuma M, Okada S, Nakamura M, Ohkawa Y, Tachibana T (2010) Rat monoclonal antibody specific for the chromatin remodelling factor, CHD1. *Hybridoma (Larchmt)* **29:** 237–240

Zhang Y, Liu T, Meyer CA, Eeckhoute J, Johnson DS, Bernstein BE, Nussbaum C, Myers RM, Brown M, Li W, Liu XS (2008) Model-based analysis of ChIP-Seq (MACS). *Genome Biol* **9:** R137

OPEN ACCESS Freely available online

PLoS one

Intra-Aortic Clusters Undergo Endothelial to Hematopoietic Phenotypic Transition during Early Embryogenesis

Chiyo Mizuochi[1], Stuart T. Fraser[2], Katia Biasch[3], Yuka Horio[1], Yoshikane Kikushige[4], Kenzaburo Tani[5], Koichi Akashi[4], Manuela Tavian[3], Daisuke Sugiyama[1]*

1 Department of Hematopoietic Stem Cells,SSP Stem Cell Unit,Kyushu University Faculty of Medical Sciences, Fukuoka, Japan, **2** Laboratory of Blood Cell Development, Disciplines of Physiology, Anatomy and Histology, School of Medical Sciences, University of Sydney, Camperdown, New South Wales, Australia, **3** Unité 682 INSERM, Strasbourg, France, **4** Department of Medicine and Biosystemic Science, Kyushu University Graduate School of Medical Sciences, Fukuoka, Japan, **5** Department of Molecular Genetics, Medical Institute of Bioregulation, Kyushu University, Fukuoka, Japan

Abstract

Intra-aortic clusters (IACs) attach to floor of large arteries and are considered to have recently acquired hematopoietic stem cell (HSC)-potential in vertebrate early mid-gestation embryos. The formation and function of IACs is poorly understood. To address this issue, IACs were characterized by immunohistochemistry and flow cytometry in mouse embryos. Immunohistochemical analysis revealed that IACs simultaneously express the surface antigens CD31, CD34 and c-Kit. As embryos developed from 9.5 to 10.5 dpc, IACs up-regulate the hematopoietic markers CD41 and CD45 while down-regulating the endothelial surface antigen VE-cadherin/CD144, suggesting that IACs lose endothelial phenotype after 9.5 dpc. Analysis of the hematopoietic potential of IACs revealed a significant change in macrophage CFC activity from 9.5 to 10.5 dpc. To further characterize IACs, we isolated IACs based on CD45 expression. Correspondingly, the expression of hematopoietic transcription factors in the CD45(neg) fraction of IACs was significantly up-regulated. These results suggest that the transition from endothelial to hematopoietic phenotype of IACs occurs after 9.5 dpc.

Citation: Mizuochi C, Fraser ST, Biasch K, Horio Y, Kikushige Y, et al. (2012) Intra-Aortic Clusters Undergo Endothelial to Hematopoietic Phenotypic Transition during Early Embryogenesis. PLoS ONE 7(4): e35763. doi:10.1371/journal.pone.0035763

Editor: Alfons Navarro, University of Barcelona, Spain

Received March 3, 2011; **Accepted** March 22, 2012; **Published** April 27, 2012

Funding: This research was supported in part by the Project for Realization of Regenerative Medicine, Special Coordination Funds for Promoting Science and Technology of the Ministry of Education, Science, Sports and Culture (www.mext.go.jp/english); and SAKURA program of the Japan Society for the Promotion of Science (www.jsps.go.jp/english/index.html). The funders had no role in study design, data collection and analysis, decision to publish, or preparation of the manuscript.

Competing Interests: The authors have declared that no competing interests exist.

* E-mail: ds-mons@yb3.so-net.ne.jp

Introduction

During mouse embryogenesis, hematopoiesis begins at the extra-embryonic yolk sac (YS) at 7.5 days post-coitum (dpc) and shifts to fetal liver after mid-gestation, then to spleen and finally to bone marrow shortly before birth. There are two distinct waves of hematopoietic emergence: a transient wave, primarily restricted to erythropoiesis in YS blood islands prior to the connection of the circulation from the YS to the embryo; and a definitive wave originating in both the YS and embryo proper. The embryonic site has been identified in the aortic region, in the para-aortic splanchnopleura (p-Sp)/aorta-gonad-mesonephros (AGM) region [1–6]. Functional hematopoietic stem cells (HSCs) that can reconstitute adult recipients are first identified in the AGM region at 10.5 dpc after ex vivo organ culture [7]. The cells at 10.5 dpc that were not cultured ex vivo rarely reconstitute adult recipients, whereas those at 11.5 dpc can regardless [7–9]. Therefore, the cells that acquire HSC activity after culture step, have been termed "pre-HSC"s. Although several reports characterize the surface marker expression on both pre-HSCs at 10.5 dpc and HSCs at 11.5 dpc, the developmental process of HSC generation still remains unclear [8–11]. Cell populations capable of reconstituting neonatal recipients are detected in the p-Sp/AGM region at 9.5 dpc [12–13]. These observations suggest that ancestor cells of HSC from the p-Sp/AGM region at 9.5 dpc require special microenvironments to acquire HSC activity and that HSCs undergo phenotypic changes from 9.5 to 10.5 dpc. In the AGM region, intra-aortic/arterial clusters (IACs) are observed attached to floors of large arteries in several species including chicken, mouse and humans [3]. Mouse IACs have been characterized morphologically and are primarily located in three large arteries, namely, the dorsal aorta (DA), the omphalomesenteric (vitelline) artery (OMA; VA) and the umbilical artery (UA) [3,14–15]. IACs express both hematopoietic (CD41 and CD45) and endothelial (CD31, CD34 and VE-cadherin) surface markers [3,15–16] suggesting that IACs are likely equivalent to ancestor cells of HSC and/or pre-HSCs and are derived from endothelial cells (ECs) at aortic/arterial regions. Although recent genetic approaches and novel tracing methods demonstrate that IACs are derived from ECs in zebrafish and mice, it is unclear how IACs form and acquire HSC activity [17–25].

To address how IACs form and function in HSC generation, we first visualized IACs by immunohistochemistry and confocal imaging and were found to simultaneously express CD31, CD34 and c-Kit. This approach enabled us to investigate the phenotypic

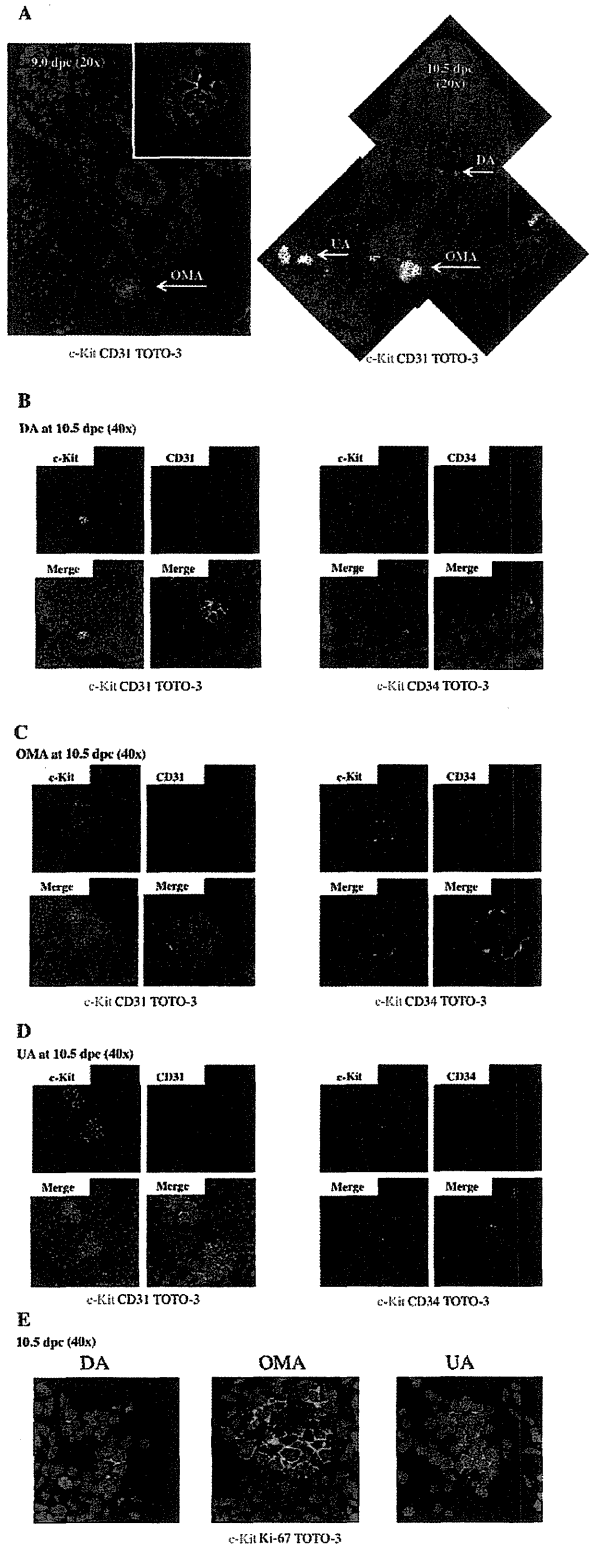

Figure 1. Confocal images of IACs expressing CD31/CD34/c-Kit in the AGM region. Transverse sections of AGM region from ICR mouse embryos at 9.0 and 10.5 dpc were stained with antibodies and observed by confocal microscopy. (**A**) IACs were observed in the omphalomesenteric artery (OMA) at 9.0 dpc (left; magnified view of IACs in upper right panel) and in the OMA, dorsal aorta (DA) and umbilical artery (UA) at 10.5 dpc (right). CD31 (red), c-Kit (green), and TOTO-3 (blue). Arrows indicate IACs. Original magnification is 20x. (**B-D**) IACs were observed in the DA (B), OMA (C) and UA (D) at 10.5 dpc. Left panel shows staining for CD31 (red), c-Kit (green), and TOTO-3 (blue), and right panel shows staining for CD34 (red), c-Kit (green), and TOTO-3 (blue) staining. Images were taken at 40x and zoom was used to show a detail at right lower panel. Another IAC in the DA is shown in Figure S1. (**E**) IACs expressing Ki-67, a marker of proliferation, were observed in the DA (left), OMA (middle) and UA (right). Ki-67 (red), c-Kit (green), and TOTO-3 (blue). Images were taken at 40x and zoom was used to show a detail.
doi:10.1371/journal.pone.0035763.g001

characterization of IACs by flow cytometry and hematopoiesis assays. Here, we demonstrate a significant transition from endothelial to hematopoietic cell phenotype of IAC cells after 9.5 dpc.

Results

Visualization of IACs in mouse embryos

Previous studies identified intra-aortic/arterial clusters (IACs) primarily by immunocytochemistry and microscopy [3,14–15]. Recently, we successfully visualized hematopoietic cell clusters in mouse placenta using thick (20 μm) cryo-sections and antibodies recognizing the embryonic HSC markers c-Kit, CD31 and CD34 and applied this method to quantifying IACs [26]. Cell aggregates consisting of more than three c-Kit-positive cells were defined as an IAC. Here, we used confocal microscopy to expand upon our previous study and characterize the cell types found within IACs according to c-Kit, CD31 and CD34 expression (Figure 1). The first IACs were observed as spherical structures in the omphalomesentric artery (OMA) at 9.0 dpc (12–14 somite pairs [SP]) (Figure 1A, left). Between 9.5 dpc (18–22 SP) to 10.5 dpc (30–34 SP), large arteries such as the dorsal aorta (DA), OMA and umbilical artery (UA) form [14]. IACs were observed in DA, OMA and UA at 10.5 dpc, and the size of IACs in the OMA and UA was significantly larger than those seen in the DA (Figure 1A, right). Localization of IACs in DA was not restricted to the ventral wall of DA, but rather some IACs were observed at dorsal and lateral sides of the wall (data not shown). All IACs in the DA, OMA and UA at 10.5 dpc simultaneously expressed c-Kit, CD31 and CD34 (Figure 1B-D). IACs expressing c-Kit in the different arteries analyzed were also positive for Ki-67, a marker of cell proliferation, regardless of location, suggesting that cells within IACs are highly proliferative (Figure 1E).

Characterization of IACs by flow cytometry and hematopoietic progenitor assays

To further characterize IACs, the caudal portion of embryos containing the p-Sp/AGM region was dissociated and analyzed by flow cytometry. At 10.5 dpc, c-Kit$^+$/CD31$^+$/CD34$^+$ cells, which are equivalent to IACs, were assessed for expression of the cell surface markers VE-cadherin/CD144 (an endothelial cell marker), CD41 (the earliest hematopoietic cell marker), CD45 (a pan-leukocyte marker), Sca-1 (a late fetal and adult HSC marker) and CD150 and EPCR (adult HSC markers) (Figure 2A-H). c-Kit$^+$/CD31$^+$/CD34$^+$ cells represented 0.069±0.01% in whole caudal portion of embryos. Among c-Kit$^+$/CD31$^+$/CD34$^+$ cells, VE-cadherin surface antigen expression decreased significantly within 24 hours from 9.5 to 10.5 dpc. Concomitantly, expression of the hematopoietic markers CD41 and CD45 increased from negative or low levels of expression on IAC cells at 9.5 dpc to abundant

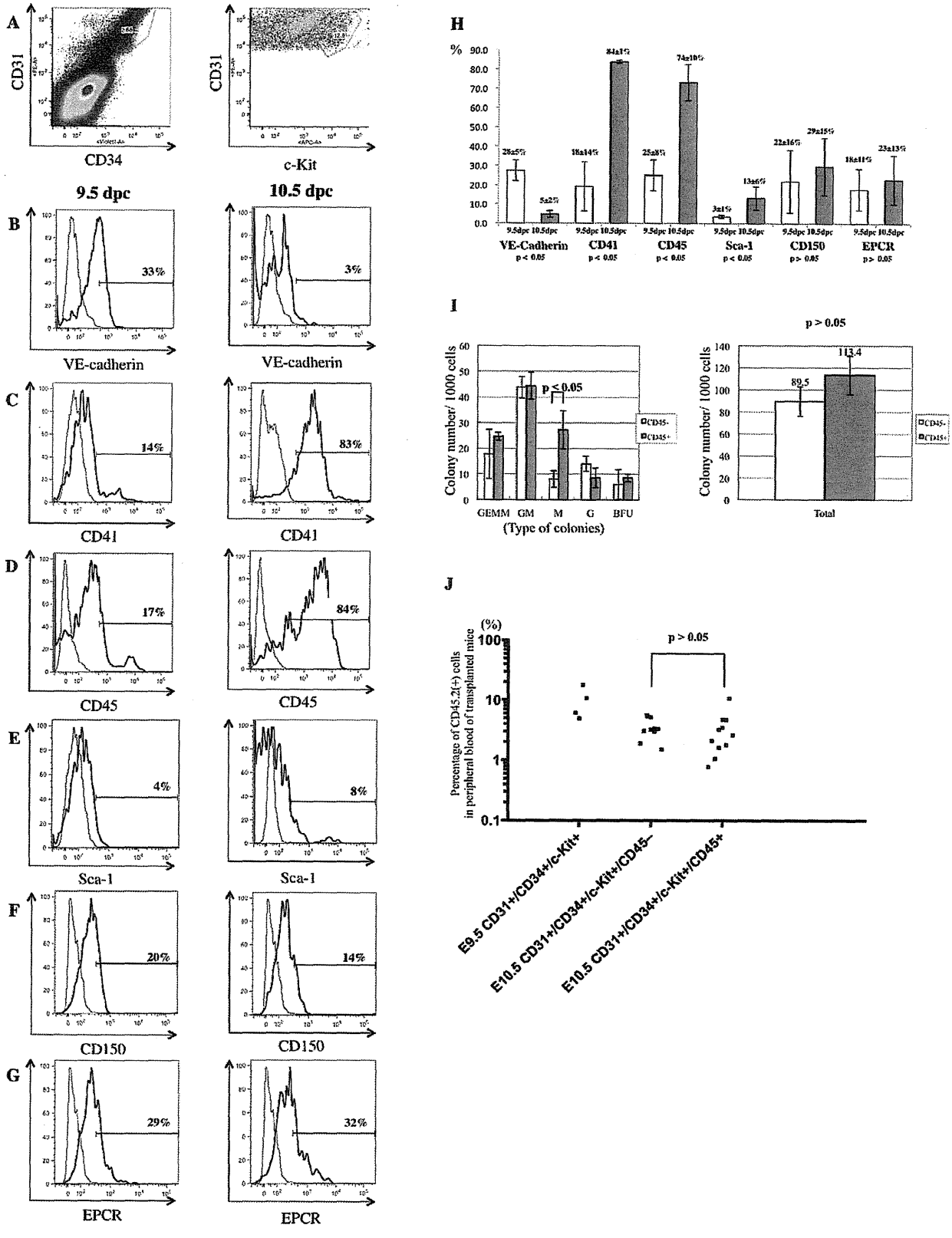

Figure 2. Flow cytometric analysis of CD31$^+$/CD34$^+$/c-Kit$^+$ AGM cells using surface expression of hematopoietic and endothelial cell markers. Single cell suspensions of the caudal portion of embryos containing the p-Sp/AGM region at 9.5 and 10.5 dpc were prepared and analyzed by flow cytometry. (**A**) Cells expressing CD31, CD34 and c-Kit markers of IACs were gated first. Isotype control of flow cytometric analysis is shown in

Figure S2. (**B-G**) Expression of hematopoietic and endothelial cell markers was analyzed on CD31$^+$/CD34$^+$/c-Kit$^+$ cells at 9.5 dpc (left) and 10.5 dpc (right) with the following antibodies: (**B**) VE-cadherin/CD144 (an endothelial cell marker), (**C**) CD41 (the earliest hematopoietic cell marker), (**D**) CD45 (a pan-leukocyte marker), (**E**) Sca-1 (a late fetal and adult HSC marker), (**F**) CD150 and (**G**) EPCR (adult HSC markers). At least 1,000 cells were assessed for each surface antigen. Representative profiles are shown. (**H**) Percentage of expression was summarized. At least 3 independent experiments were performed. Mean ± 2SD was calculated and shown at the top of bars. (**I**) One thousand sorted CD45-negative or CD45-positive CD31$^+$/CD34$^+$/c-Kit$^+$ cells were cultured in semisolid medium containing the hematopoietic cytokines, SCF (Stem Cell Factor), IL (Interleukin)-3, IL-6 and EPO (Erythropoietin). Left and right panels show each fraction and the total number of colonies, respectively. GEMM (colony-forming units of granulocyte erythrocyte monocyte macrophages); GM (of granulocyte macrophages); M (of macrophages); G (of granulocytes); BFU (burst forming units of erythroid cells). (**J**) 50–100 sorted CD31$^+$/CD34$^+$/c-Kit$^+$ cells at 9.5 dpc, as well as CD45-negative and CD45-positive CD31$^+$/CD34$^+$/c-Kit$^+$ cells were transplanted into busulfan-treated Ly5.1 mouse neonates. Approximately one year after transplantation, blood samples were collected and analyzed for CD45.2 expression by flow cytometry. Representative profile of flow cytometric analysis and its negative and positive controls are shown in Figure S3 and S6, respectively.
doi:10.1371/journal.pone.0035763.g002

levels at 10.5 dpc. Sca-1 expression also increased from 9.5 to 10.5 dpc.

We next separated c-Kit$^+$/CD31$^+$/CD34$^+$ cells based on CD45 expression by flow cytometry and performed colony assays and transplantation assays. As shown in Figure 2I (left), the number of CFU-M generated from CD45-positive c-Kit$^+$/CD31$^+$/CD34$^+$ cells (27.3) was significantly higher than CFU-M from CD45-negative c-Kit$^+$/CD31$^+$/CD34$^+$ cells (8.0) ($p<0.05$). However, the total number of hematopoietic colonies did not differ between CD45-negative and CD45-positive c-Kit$^+$/CD31$^+$/CD34$^+$ cells ($p>0.05$). When 50–100 c-Kit$^+$/CD31$^+$/CD34$^+$ cells were transplanted into neonate recipients, there was no significant difference in reconstitution ability (CD45-negative, 3.55%; CD45-positive 3.07%) ($p>0.05$) (Figure 2J). c-Kit$^+$/CD31$^+$/CD34$^+$ cells at 9.5 dpc were able to reconstitute recipients and chimerism to 9.89% was achieved. Presumptive ancestor cells of HSC can reportedly reconstitute neonate recipients but not adult recipients [13]. In addition, pre-HSCs at 10.5 dpc rarely reconstitute adult recipients without culture step [7–9,11]. When 100 c-Kit$^+$/CD31$^+$/CD34$^+$ cells were transplanted into adult recipients, no reconstitution was observed (data not shown).

Expression of CD45 in mouse and human intra-aortic/arterial clusters

CD45-negative and CD45-positive c-Kit$^+$/CD31$^+$/CD34$^+$ cells showed no difference in hematopoietic potential except within the macrophage lineage. To further investigate a role of CD45 expression on c-Kit$^+$/CD31$^+$/CD34$^+$ cells, we used flow cytometry to segregate c-Kit$^+$/CD31$^+$/CD34$^+$ cells into three fractions. Three distinct populations became apparent; CD45negative cells, CD45low cells, and CD45high cells (Figure 3A). The proportion of CD45-negative and CD45-low positive c-Kit$^+$/CD31$^+$/CD34$^+$ cells was higher at 9.5 dpc than at 10.5 dpc, whereas the percentage of CD45-high positive c-Kit$^+$/CD31$^+$/CD34$^+$ cells increased by 5-fold at 10.5 dpc (31.0%) compared to 9.5 dpc (6.3%) (Figure 3B). These data suggest that CD45-negative c-Kit$^+$/CD31$^+$/CD34$^+$ cells are precursors of CD45-high positive c-Kit$^+$/CD31$^+$/CD34$^+$ cells and that CD45 is a marker of IAC maturation. To address this issue, we examined expression levels of the gene encoding CD45 (*Ptprc; protein tyrosine phosphatase, receptor type, C*) and of various hematopoietic transcription factors (Runx1, c-Myb, Evi-1, SCL and Gata2) (Figure 3C-H). CD45-negative c-Kit$^+$/CD31$^+$/CD34$^+$ cells expressed low levels of *CD45* mRNA. *Ptprc* transcript levels increased significantly as CD45 surface protein expression was up-regulated in the c-Kit$^+$/CD31$^+$/CD34$^+$ population. Expression levels of all hematopoietic transcription factor genes assayed except *Evi-1* was highest in CD45-low positive c-Kit$^+$/CD31$^+$/CD34$^+$ cells. In agreement with flow cytometric analysis, evaluation of CD45 protein expression by immunohistochemistry indicated that IACs in the OMA at 9.5 dpc were CD45-negative while some IACs in the DA, OMA and UA were CD45-positive by 10.5 dpc (Figure 4A-D).

IAC formation in the developing human embryo is poorly defined. Having defined the developmental progression of IAC in the mouse above, we next examined IAC morphology and phenotype in a 32 day-old human embryo. Immunohistochemistry of embryonic human cryosections was performed using anti-human CD34 and CD45 antibodies. As shown in Figure 4E, IACs can be detected in ventral wall of the dorsal aorta. CD34 was expressed by a wide range of vascular endothelial cells throughout the embryo. CD45 was restricted to round and in many cases clearly circulating cells. However, within the IAC observable on the ventral wall of the dorsal aorta, cells expressing both CD34 and CD45 can be seen. This reflects the expression pattern we have identified in embryonic mouse IACs.

Transcription factor hierarchy in IAC development

We next observed IAC formation by immunohistochemistry and flow cytometry in mouse embryos harboring mutations associated with aberrant embryonic hematopoiesis [27–32]. Immunohistochemical analysis of *Runx1*$^{-/-}$ embryos lacked IACs in the DA, OMA and UA. Flow cytometric analyses confirmed the absence of c-Kit$^+$/CD31$^+$/CD34$^+$ cells in *Runx1*$^{-/-}$ embryos compared to wild type embryos (Figure 5A-B). *Evi-1*$^{-/-}$ embryos also lacked IACs in the DA, OMA and UA by immunohistochemistry. However, a small frequency of c-Kit$^+$/CD31$^+$/CD34$^+$ cells could be detected by flow cytometry (Figure 5C). In *c-Myb*$^{-/-}$ embryos, IACs were observed at the DA, OMA and UA, and c-Kit$^+$/CD31$^+$/CD34$^+$ cells were also observed by flow cytometry (Figure 5D). Collectively, these results demonstrate that Runx1 is essential for IAC formation while Evi-1 appears to be playing a function downstream of Runx1 in this process.

Discussion

During embryogenesis, a unique cell biological shift takes places in which endothelial cells with adherens junctions detach from each other, alter gene expression and become hematopoietic cells. This process is limited both anatomically and temporally. We here demonstrated that the transition from endothelial to hematopoietic phenotype of IACs occurs from 9.5 dpc in the mouse embryo, earlier than previously described. Furthermore, we show that IACs are identifiable in the human embryo based on CD45 expression, implying that this process in mice is applicable to human.

Previously, we reported an immunohistochemistry visualization technique revealing hematopoietic cell clusters in placenta using thick (20 μm) cryo-sections and antibodies recognizing embryonic HSC markers [26]. Here, we applied this technique to obtain high quality confocal images of intra-aortic/arterial clusters (IACs) in the AGM region. We defined IACs as c-Kit$^+$/CD31$^+$/CD34$^+$ cells. Recently, c-Kit$^+$/CD31$^+$/SSEA-1$^-$ cells were also identified in the AGM region [11]. As CD31 is expressed on both IACs and primordial germ cells (PGCs), it was necessary to exclude PGCs according to SSEA-1 expression. As shown in Figure 2 and 5, we

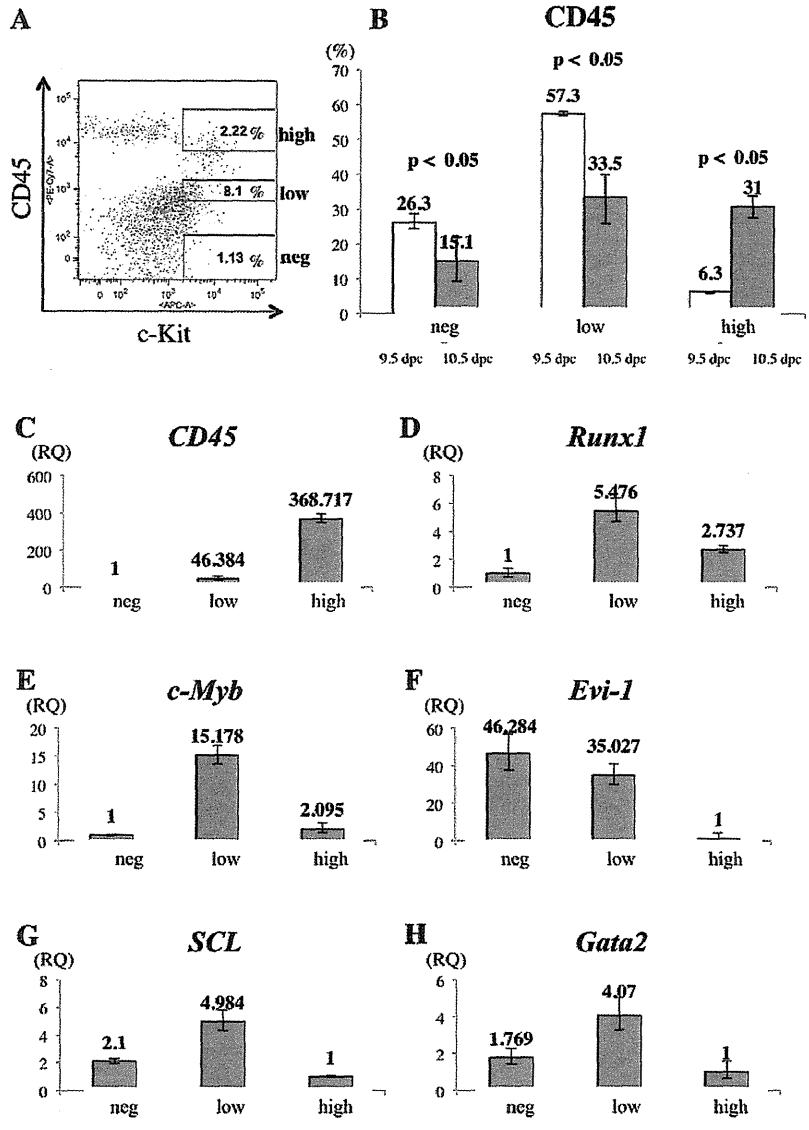

Figure 3. Gene expression analysis in CD31$^+$/CD34$^+$/c-Kit$^+$ AGM cells separated by CD45 expression. (**A**) Single cell suspensions of the caudal portion of embryos containing the AGM region at 10.5 dpc were prepared and analyzed by flow cytometry. Cells expressing CD31 and CD34, IAC markers, were first gated. The profile shows expression of c-Kit (x-axis) and CD45 (y-axis) in CD31$^+$/CD34$^+$ AGM cells (left). Based on intensity of CD45 expression, CD31$^+$/CD34$^+$/c-Kit$^+$ AGM cells were separated into three fractions, CD45-negative (under 10^2 of CD45-fluorescence, same as negative control), -low positive (from $10^{2.5}$ to $10^{3.5}$ of CD45-fluorescence), and -high positive (approximately over 10^4 of CD45-fluorescence). Isotype control and compensation samples of flow cytometric analysis are shown in Figure S4 and S5. (**B**) The percentage of CD45-negative, -low positive, and -high positive c-Kit$^+$/CD31$^+$/CD34$^+$ AGM cells was calculated both at 9.5 dpc (white bars) and 10.5 dpc (black bars). (**C-H**) Gene expression of *CD45* (C), *Runx1* (D), *c-Myb* (E), *Evi-1* (F), *SCL* (G) and *Gata2* (H) was analyzed in sorted CD45-negative, -low positive and -high positive c-Kit$^+$/CD31$^+$/CD34$^+$ AGM cells. Expression levels of *CD45* mRNA are up-regulated as c-Kit$^+$/CD31$^+$/CD34$^+$ cells express CD45 surface protein. Expression levels of *Runx1*, *c-Myb*, *Evi-1*, *SCL* and *Gata2* were highest in CD45-low positive c-Kit$^+$/CD31$^+$/CD34$^+$ cells, whereas that of *Evi-1* was highest in CD45-negative c-Kit$^+$/CD31$^+$/CD34$^+$ cells. RQ represents relative quantity of template in the original sample.
doi:10.1371/journal.pone.0035763.g003

could observe a small number of CD31$^+$/CD34$^-$ cells, which are likely to be PGCs. Since PGCs do not express CD34 at this stage, we could positively select the IAC fraction based on our definition by flow cytometry [33]. Our observation of IACs is compatible with the result showing large IACs were primarily observed in omphalomesentric artery (OMA) and umbilical artery (UA) at 10.5 dpc [11]. In the mouse, IACs protruding into the lumen of arteries were previously reported at 9.5 dpc in studies using microscopy and Tie-2 immunohistochemistry [14,34]. Prior to 9.5 dpc, we identified the first IACs, which formed a spherical structure, in the OMA at 9.0 dpc (Figure 1A). The OMA appears at 8.0 dpc and directly connects with the dorsal aorta (DA). The OMA anastomoses with the DA after 9.5 dpc and loses its connection with the UA by 10.5 dpc [14,35]. Our data (Figure 1E) indicate that IACs are proliferative, based on Ki-67 staining. Taken together, it is likely that the first IACs in the OMA proliferate and are distributed into

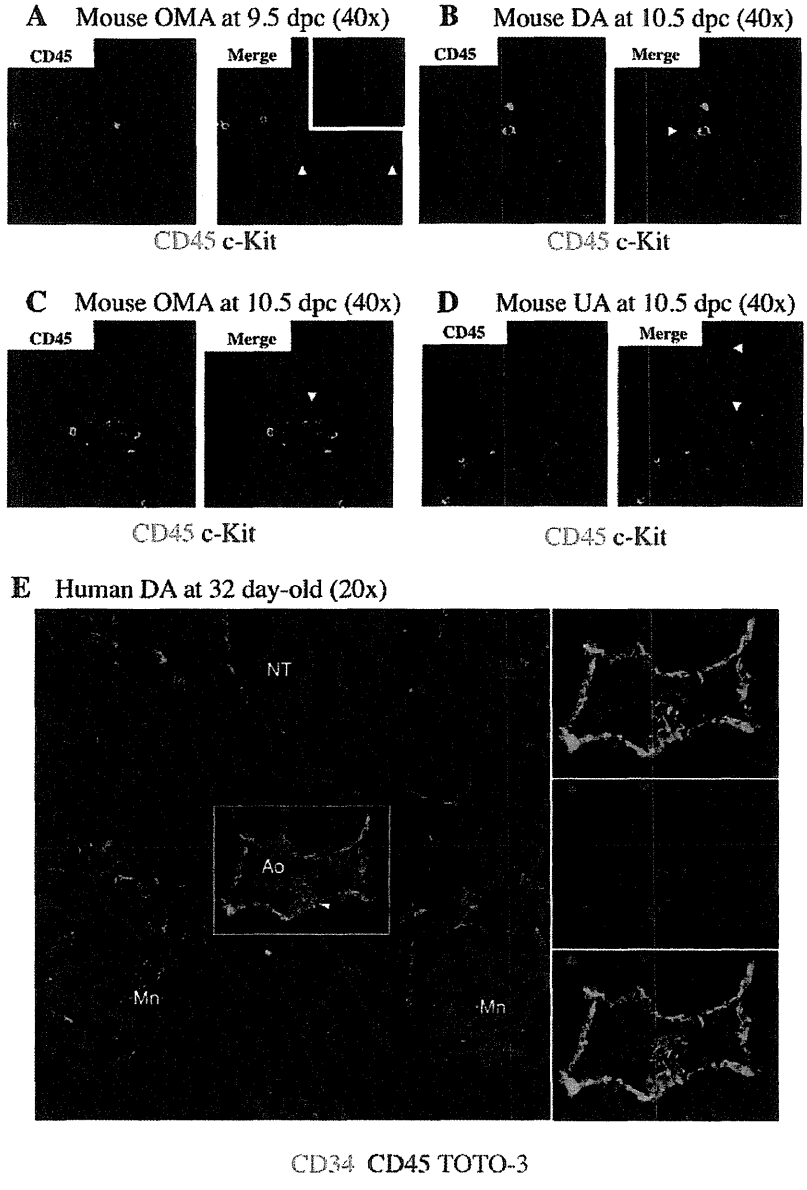

Figure 4. Expression of CD45 by mouse and human IACs. Transverse sections of AGM region were made from ICR mouse embryos at 9.5 and 10.5 dpc and from human embryos at 32 day-old, according to the Carnegie classification, stained with antibodies and observed by confocal microscopy. Arrowheads indicate IACs. (**A**) Mouse IACs in the omphalomesenteric artery (OMA) at 9.5 dpc expressed c-Kit, but not CD45. CD45 (green) and c-Kit (red). Magnified view of IACs is shown at right upper panel in Merge panel. Original magnification is 40x. (**B-D**) Mouse IACs in the dorsal aorta (DA) (B), OMA (C) and umbilical artery (UA) (D) at 10.5 dpc expressed c-Kit, and some expressed CD45. CD45 (green) and c-Kit (red). Original magnification is 40x. (**E**) All human IACs in the DA expressed CD34, and some expressed CD45. CD34 (green), CD45 (red) and TOTO-3 (blue). NT (Neural Tube); Ao (Aorta); Mn (Mesonephros). Original magnification is 20x.
doi:10.1371/journal.pone.0035763.g004

large arteries, such as the DA and UA, as the arterial system develops. Although several reports provide direct evidence that endothelial cells (ECs) generate IACs, we cannot rule out the possibility that either mesodermal cells, the ancestors of hematopoietic cells, or so-called hemangioblasts, which give rise both to ECs and hematopoietic cells, generate IACs by another pathway [17–25]. When VE-cadherin^{+}/CD45^{-} cells were sorted out from AGM regions at 10.5 dpc, and co-aggregated with OP9 stromal cells, these cells acquired HSC activity [8]. As embryos develop, VE-cadherin^{+}/CD45^{+} cells from AGM regions at 11.5 dpc can reconstitute adult recipients without culture step, whereas both VE-cadherin^{+}/CD45$^{+/-}$ cells can after aggregation culture with OP9 stromal cells. It suggests that the transition from endothelial to hematopoietic phenotype in pre-HSCs occurs between 10.5 and 11.5 dpc. According to our flow cytometric analysis of IACs, the transition from endothelial to hematopoietic phenotype occurs after 9.5 dpc (Figure 2). Although we found that 33% of c-Kit^{+}/CD31^{+}/CD34^{+} cells at 9.5 dpc express VE-cadherin, most IACs defined as

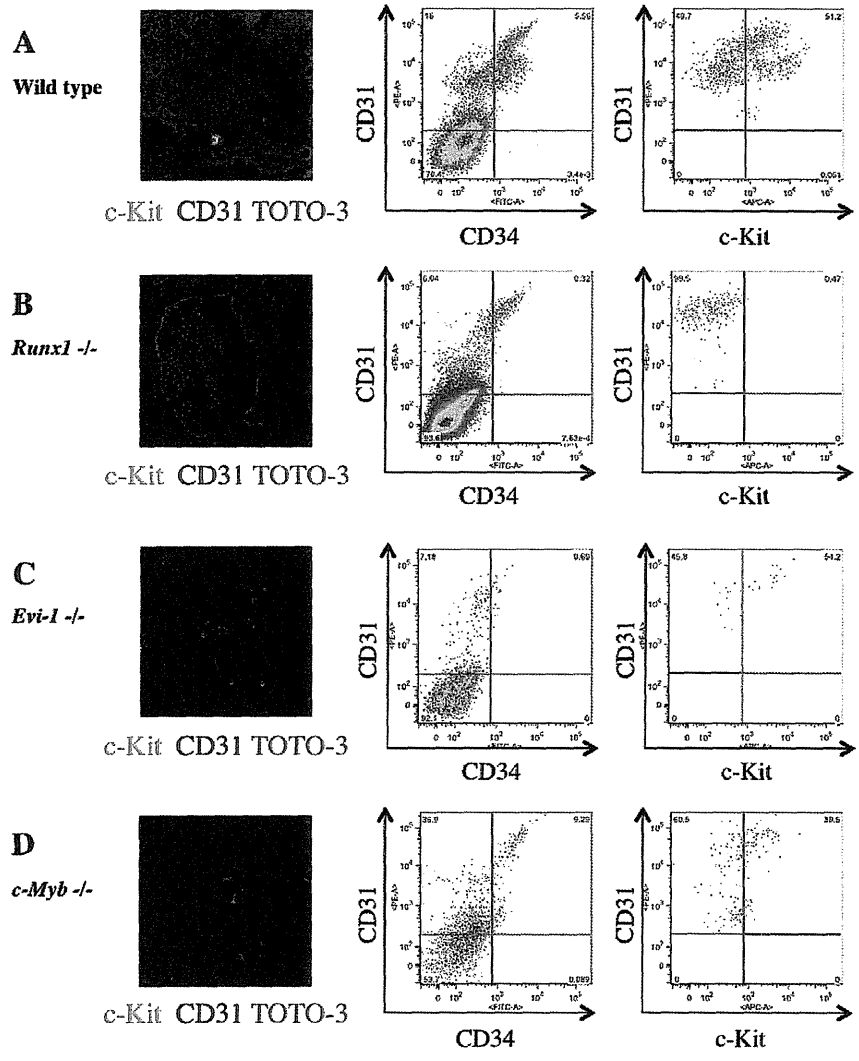

Figure 5. Altered IAC phenotype in *Runx1*$^{-/-}$, *Evi-1*$^{-/-}$ and *c-Myb*$^{-/-}$ embryos. Transverse sections of the AGM region were made from ICR, *Runx1*$^{-/-}$, *Evi-1*$^{-/-}$ and *c-Myb*$^{-/-}$ mouse embryos at 10.5 dpc, stained with antibodies and observed by confocal microscopy. Single cell suspensions of AGM regions from these embryos at 10.5 dpc were prepared and analyzed by flow cytometry. (**A-D**) Left panels show confocal images stained with anti-c-Kit (green) and CD31 (red) antibodies and TOTO-3 (blue). Middle and right panels show flow cytometric profiles of CD34 (x-axis) and CD31 (y-axis), and c-Kit (x-axis) and CD31 (y-axis), respectively. Isotype control and compensation samples of flow cytometric analysis are shown in Figure S2 and S5. (**A**) ICR mouse embryos serve as (wild type) controls. IACs and CD31^{+}/CD34^{+}/c-Kit^{+} AGM cells were observed. (**B**) No IACs were observed in *Runx1*$^{-/-}$ embryos, whereas the aortic structure was conserved (left). No CD31^{+}/CD34^{+}/c-Kit^{+} AGM cells were observed, whereas CD31^{+}/CD34^{+}/c-Kit^{-} AGM cells, which are equivalent to ECs, were observed (middle and right). (**C**) No IACs were observed and aortic structure was altered in *Evi-1*$^{-/-}$ embryos (left). CD31^{+} AGM cells were observed, but they did not express CD34 and c-Kit (middle and right). (**D**) IACs were observed in *c-Myb*$^{-/-}$ embryos and the aortic structure was conserved (left). CD31^{+}/CD34^{+}/c-Kit^{+} AGM cells were observed (middle and right).
doi:10.1371/journal.pone.0035763.g005

c-Kit^{+}/CD31^{+}/CD34^{+} cells by flow cytometry did not contribute to blood vessel structure. VE-cadherin is expressed in IACs as well as in ECs [16]. It is likely that sorted VE-cadherin^{+}/CD45^{-} cells from AGM regions at 10.5 dpc contained ECs with HSC potential in addition to some IACs. Further studies are necessary to determine how ECs contribute to IAC generation. CD150 belongs to the SLAM family and its expression is developmentally regulated on the surface of HSCs. At 11.5 dpc, CD150^{-} cells can reconstitute adult recipients, but CD150^{+} cells not [10]. In this study, CD150 expression was examined on c-Kit^{+}/CD31^{+}/CD34^{+} cells by flow cytometry and the percentage of CD150 expression was not changed (Figure 2F, H). It will be interesting to compare the CD150 expression between 10.5 and 11.5 dpc.

The pan-leukocyte marker CD45 is a transmembrane glycoprotein that functions as a protein phosphotyrosine phosphatase. Although loss of the *CD45* gene results in T and B lymphocyte anomalies in adult, there appears to be no significant abnormality in HSC development during embryogenesis [36–38]. We observed that CD45 protein expression was up-regulated in c-Kit^{+}/CD31^{+}/CD34^{+} cells between 9.5 and 10.5 dpc (Figure 2D). Our results are compatible with the report showing that CD45 is expressed on the surface of IACs at 10.5 dpc, but not on the IACs at 9.5 dpc [11].

In agreement with previous reports, we observed no significant differences in HSC activity based on neonatal transplantation, whereas myeloid potential differs based on colony formation assay between CD45-negative and CD45-positive c-Kit$^+$/CD31$^+$/CD34$^+$ cells, suggesting that CD45 expression is not required for hematopoietic cell identity (Figure 2I, J) [39–40]. However, pre-HSCs that can reconstitute both adult and neonatal recipients appear at 10.5 dpc, whereas presumptive ancestor cells of HSC that can reconstitute only neonatal but not adult recipients appear at 9.5 dpc [7,12–13]. In accordance with flow cytometric data, some IACs expressed CD45 while others did not in both 10.5 dpc mouse embryos and 32 day-old human embryos (Figure 4B-E). Taken together, although CD45 does not function in HSC development, its expression on the cell surface might serve as a marker of pre-HSC maturation from ancestor cells of HSC. With regard to myeloid potential, only macrophage development differs (Figure 2I). At 10.5 dpc, macrophages are reportedly c-Kit$^-$/CD31$^+$/CD45$^+$ cells, and we could observe some c-Kit$^-$/CD45$^+$ cells in the AGM regions (Figure 4) [11]. CD45 expression on c-Kit$^+$/CD31$^+$/CD34$^+$ cells might be the diverging point of myeloid potential. Furthermore, we identified *CD45* gene expression in CD45-negative c-Kit$^+$/CD31$^+$/CD34$^+$ cells, suggesting that these cells are primed to differentiate into CD45-positive c-Kit$^+$/CD31$^+$/CD34$^+$ cells. Expression levels of *Runx1, c-Myb, SCL* and *Gata2* were highest in CD45-low positive c-Kit$^+$/CD31$^+$/CD34$^+$ cells, implying that the transition from endothelial to hematopoietic phenotype of IACs occurs in CD45-low positive c-Kit$^+$/CD31$^+$/CD34$^+$ cells, as these transcription factors are reportedly important for the switch to hematopoietic cells [22]. Evi-1 is involved in vasculo-angiogenesis in addition to HSC development [31]. Therefore, high expression level of *Evi-1* gene in CD45-negative c-Kit$^+$/CD31$^+$/CD34$^+$ cells implies that this population still preserves some endothelial identity.

We also investigated IACs from *Runx1*$^{-/-}$, *Evi-1*$^{-/-}$ or *c-Myb*$^{-/-}$ mouse embryos. Runx1 is essential for definitive hematopoiesis, and its expression marks the site of *de novo* generation of definitive hematopoietic cells [28–30]. In agreement with previous reports, we observed an absence of IACs in *Runx1*$^{-/-}$ mouse embryos. *Evi-1*$^{-/-}$ mouse embryos displayed abnormalities in vascular and hematopoietic development [31–32]. As shown in Figure 5C, *Evi-1*$^{-/-}$ mouse embryos comprised a few c-Kit$^+$/CD31$^+$/CD34$^+$ cells based on flow cytometric analysis. High expression of *Evi-1* in CD45-negative c-Kit$^+$/CD31$^+$/CD34$^+$ cells may correlate with vascular development and impairment of IAC formation. c-Myb is essential for HSC maturation and proliferation, and *c-Myb*$^{-/-}$ mouse embryos die at 15.5 dpc from impaired definitive hematopoiesis in fetal liver, although primitive hematopoiesis appears normal [27]. In contrast to *Runx1*$^{-/-}$ or *Evi-1*$^{-/-}$ mouse embryos, *c-Myb*$^{-/-}$ mouse embryos exhibited IACs.

Several evidences reveal that HSCs are generated from ECs [17–21]. Taken together, our results corroborate HSC-generation from ECs and imply that IACs gradually acquire hematopoietic phenotype after 9.5 dpc. Understanding how IACs are generated could lead to an understanding of how to manipulate HSC generation from ES/iPS cells and thus be applicable to future clinical applications.

Materials and Methods

Mice

Ly5.1 (Sankyo Labo Service, Tokyo, Japan) mice, Ly5.2 adult C57/BL6 mice (Kyudo, Tosu, Japan), ICR mice (SLC, Hamamatsu, Japan), *Runx1*$^{+/-}$ mice (provided by Dr. Speck at University of Pennsylvania), *Evi-1*$^{+/-}$ mice (JAX mice and Services, Bar Harbor, ME) and *c-Myb*$^{+/-}$ mice (JAX mice and Services) were used in these studies. To analyze cells, pregnant mice were sacrificed at 9.0–10.5 dpc and somite pair number was counted. Embryos at 9.0 dpc with 12–14 somite pairs (SP), 9.5 dpc with 18–22 SP and 10.5 dpc with 30–34 SP were dissected out, respectively. Animals were handled according to the Guidelines for the Care and Use of Laboratory Animals of Kyushu University. This study was approved by Animal Care and Use Committee, Kyushu University (Approval ID: A21-068-0).

Mouse immunohistochemistry

Embryos were dissected out and fixed in 2% paraformaldehyde in PBS, followed by equilibration in 30% sucrose in PBS. Embryos were embedded in OCT compound (SAKURA, Tokyo, Japan) and frozen in liquid nitrogen. Tissues were sliced at 20 μm on a Leica CM1900 UV cryostat, transferred to glass slides (Matsunami, Osaka, Japan) and dried thoroughly. Sections were blocked in 1% BSA in PBS and incubated in PBS containing 1% BSA with appropriate dilutions of the following primary antibodies: goat anti-mouse c-Kit (R&D Systems, Minneapolis, MN), rat anti-mouse CD31 (BD Biosciences, San Diego, CA), rat anti-mouse CD34 (BD Biosciences), rat anti-mouse CD45 (Biolegend) and rat anti-mouse Ki-67 antigen (Dako Corporation, Carpinteria, CA) at 4C overnight. After washing in PBS three times, sections were incubated with appropriate dilutions of the following secondary antibodies: Alexa Fluor 488 donkey anti-rat IgG (Invitrogen, Carlsbad, CA), Alexa Fluor 488 donkey anti-goat IgG (Invitrogen), Alexa Fluor 546 donkey anti-goat IgG (Invitrogen) and Alexa Fluor 568 donkey anti-goat IgG (Invitrogen), as well as TOTO-3 (Invitrogen) to stain nuclei, at room temperature for 30 minutes. Samples were mounted on coverslips using fluorescent mounting medium (Dako Corporation) and assessed using a FluoView 1000 confocal microscope (Olympus, Tokyo, Japan).

Human tissues

Human embryos were obtained from voluntary abortions performed according to guidelines and with the approval of the French National Ethics Committee. In all cases, written consent allowing use of the embryo for research was obtained from the patient. Developmental age was estimated based on anatomical criteria and the Carnegie classification as previously described [41–42].

Human immunohistochemistry

Embryos were fixed overnight at 4°C in PBS plus 4% paraformaldehyde (Sigma-Aldrich), rinsed twice in PBS, then in PBS/15% sucrose (Sigma-Aldrich) for at least 24 hours. Tissues were then embedded in PBS with 15% sucrose and 7.5% gelatin (Sigma-Aldrich), frozen and stored at -80°C. Frozen sections (5 μm) were stored at −20°C until use, and then thawed and hydrated in PBS [37]. For double-staining, the TSA Plus Fluorescence amplification system was used, according to the manufacturer's instructions (NEN-Perkin Elmer). Endogenous peroxidases were inhibited for 20 minutes in PBS containing 0.2% hydrogen peroxide (Sigma-Aldrich). Sections were washed in PBS and non-specific binding sites were blocked with PBS/5% goat serum (Vector Laboratories) for 1 hour. Sections were then incubated with uncoupled antibody to CD45 (overnight at room temperature). After rinsing, sections were incubated with biotinylated goat anti-mouse IgG antibody (Immunotech) for 1 hour and then with peroxidase-labeled streptavidin (Immunotech) for 1 hour. Staining was revealed using fluorescent tyramide (TMR, Tetramethylrhodamine). Residual peroxidase activity was inhibited in PBS/0.2% hydrogen peroxide for 10 min at RT. After 3

washings in PBS, slides were treated with an Avidin/Biotin blocking kit according to the manufacturer's instructions (Vector Laboratories). Sections were washed and incubated with anti-CD34 antibody at room temperature for 2 hours, then with biotinylated goat anti-mouse IgG antibody (Immunotech) for 1 hour at RT, and with Alexa 488-labeled streptavidin for 1 hour. Slides were mounted in Vectashield medium (Vector Laboratories). Monoclonal antibodies to CD34 (IgG1, clone Qbend-10) and CD45 (IgG1, clone Hle-1) were purchased from Immunotech and Becton-Dickinson Biosciences, respectively.

Cell preparation

The caudal portion of embryos containing the p-Sp/AGM region was used to obtain a single cell suspension. Tissues were incubated with 1 mg/ml collagenase in medium supplemented with 10% fetal bovine serum for 30 minutes at 37°C and filtered through 40-μm nylon cell strainers (BD Biosciences).

Flow cytometry and cell sorting

Antibodies used for analysis were: FITC-conjugated anti-mouse CD41 (eBioscience, San Diego, CA), FITC-conjugated anti-mouse Sca-1 (eBioscience), FITC-conjugated anti-mouse EPCR (Endothelial Protein C Receptor) known as CD201 (Stem Cell Technologies inc, Vancouver, BC), PE-conjugated anti-mouse CD31 (BD Biosciences), PE-Cy7-conjugated anti-mouse CD45 (BioLegend), APC and APC-Cy7-conjugated anti-mouse c-Kit (BD Biosciences), Aexa Fluor488-conjugated anti-mouse CD150 (BioLegend), APC-conjugated anti-mouse VE-cadherin (clone name; VECD-1, provided by Dr. Ogawa at Kumamoto University), and FITC and Pacific Blue-conjugated anti-mouse CD34 (eBioscience). Flow cytometric analysis and cell sorting were carried out using a FACSAria SORP cell sorter (BDIS, San Jose, CA). Data files were analyzed using FlowJo software (Tree Star, Inc., San Carlos, CA).

RNA extraction and real-time PCR analysis

Total RNA was isolated using the RNAqueous 4PCR kit (Ambion Inc., Austin, Texas). mRNA was reverse transcribed using a High-Capacity RNA-to-cDNA kit (Life Technologies, Carlsbad, CA). The quality of cDNA synthesis was evaluated by amplifying mouse ß-actin using PCR. Thirty thermal cycles were used as follows: denaturation at 95°C for 10 sec, annealing at 60°C for 20 sec, followed by extension at 72°C for 20 seconds. Gene expression levels were measured by real time PCR with TaqMan® Gene Expression Master Mix and StepOnePlus™ real time PCR (Life Technologies). All probes were from TaqMan® Gene Expression Assays (Life Technologies). All analyses were performed in triplicate wells; mRNA levels were normalized to ß-actin and the relative quantity (RQ) of expression was compared with a reference sample.

Colony formation assay

Sorted cells were suspended in 3 ml of MethoCult® GF M3434 (Stemcell Technologies) distributed into three 35 mm dishes and then incubated in 5% CO_2 at 37°C. Colonies were counted up 14 days later using an inverted phase contrast microscope CKX41 (Olympus, Tokyo, Japan).

Transplantation assay

To examine neonatal repopulating HSCs, sorted cells were transplanted into busulfan-treated Ly5.1 mouse neonates as described previously [9,15]. Briefly, time-pregnant mice were injected on days 17 and 18 after conception with 15 μg of busulfan/gram body weight of the mother (Sigma-Aldrich, St.Louis MO). Isolated cells were suspended in 25 μl PBS and transplanted into neonates at the time of delivery using a 100 μl Hamilton syringe (Hamilton, Reno, NV). Approximately one year after transplantation, blood samples were collected, lysed in BD Pharm Lyse (BD Biosciences) and analyzed for CD45.2 expression by flow cytometry.

Supporting Information

Figure S1 Additional confocal images of IAC expressing CD31/CD34/c-Kit in the dorsal aorta of AGM region at 10.5 dpc. Staining for CD34 (red), c-Kit (green), and TOTO-3 (blue) is shown. Original magnification is 40x.
(TIFF)

Figure S2 Single cell suspensions of the caudal portion of embryos containing the p-Sp/AGM region at 9.5 and 10.5 dpc were prepared and analyzed by flow cytometry. Upper panels show isotype control of analysis corresponding to Figure 2A. Lower panels show isotype control of analysis corresponding to Figure 5.
(TIFF)

Figure S3 50–100 sorted $CD31^-/CD34^+/c\text{-}Kit^+$ cells at 9.5 dpc, as well as CD45-negative and CD45-positive $CD31^+/CD34^+/c\text{-}Kit^+$ cells were transplanted into busulfan-treated Ly5.1 mouse neonates. Approximately one year after transplantation, blood samples were collected, lysed in lysing solution and analyzed for CD45.2 expression by flow cytometry. Representative profile of flow cytometric analysis is shown.
(TIFF)

Figure S4 Single cell suspensions of the caudal portion of embryos containing the AGM region at 10.5 dpc were prepared and analyzed by flow cytometry. The profile shows isotype control of analysis corresponding to Figure 3A. Based on the isotype control, sorting gates are set into three fractions, CD45-negative (under 10^2 of CD45-fluorescence, same as negative control), -low positive (from $10^{2.5}$ to $10^{3.5}$ of CD45-fluorescence), and -high positive (approximately over 10^4 of CD45-fluorescence).
(TIFF)

Figure S5 Single cell suspensions of the caudal portion of embryos containing the p-Sp/AGM region at 9.5 and 10.5 dpc were prepared and analyzed by flow cytometry. Compensation samples of analysis corresponding to Figure 3A and 5 were shown.
(TIFF)

Figure S6 Negative and positive controls to transplantation analysis are shown corresponding to Figure S3. Peripheral blood samples were obtained from Ly5.1 adult mouse for negative control and Ly5.2 adult C57/BL6 mice for positive control, respectively.
(TIFF)

Acknowledgments

We thank the Research Support Center, the Graduate School of Medical Sciences, Kyushu University for technical support, Drs. K. Nakao and K. Kulkeaw for technical support, and Dr. Elise Lamar for critical reading of our manuscript.

Author Contributions

Conceived and designed the experiments: DS. Performed the experiments: CM KB YH YK MT DS. Analyzed the data: CM SF KB MT DS. Contributed reagents/materials/analysis tools: CM KB MT KT KA DS. Wrote the paper: CM SF DS.

References

1. Dzierzak E, Speck NA (2008) Of lineage and legacy: the development of mammalian hematopoietic stem cells. Nat Immunol 9: 129–136.
2. Mikkola HK, Orkin SH (2006) The journey of developing hematopoietic stem cells. Development 133: 3733–3744.
3. Godin I, Cumano A (2002) The hare and the tortoise: an embryonic haematopoietic race. Nat Rev Immunol 2: 593–604.
4. Dieterlen-Lievre F, Pouget C, Bollerot K, Jaffredo T (2006) Are intra-aortic hemopoietic cells derived from endothelial cells during ontogeny? Trends Cardiovasc Med 16: 128–139.
5. Jaffredo T, Bollerot K, Sugiyama D, Gautier R, Drevon C (2005) Tracing the hemangioblast during embryogenesis: developmental relationships between endothelial and hematopoietic cells. Int J Dev Biol 49: 269–277.
6. Sugiyama D, Tsuji K (2006) Definitive hematopoiesis from endothelial cells in the mouse embryo; a simple guide. Trends Cardiovasc Med 16: 45–49.
7. Medvinsky A, Dzierzak E (1996) Definitive hematopoiesis is autonomously initiated by the AGM region. Cell 86: 897–906.
8. Taoudi S, Gonneau C, Moore K, Sheridan JM, Blackburn CC, et al. (2008) Extensive hematopoietic stem cell generation in the AGM region via maturation of VE-cadherin+CD45+ pre-definitive HSCs. Cell Stem Cell 3: 99–108.
9. Rybtsov S, Sobiesiak M, Taoudi S, Souilhol C, Senserrich J, et al. (2011) Hierarchical organization and early hematopoietic specification of the developing HSC lineage in the AGM region. J Exp Med 208: 1305–1315.
10. McKinney-Freeman SL, Naveiras O, Yates F, Loewer S, Philitas M, et al. (2009) Surface antigen phenotypes of hematopoietic stem cells from embryos and murine embryonic stem cells. Blood 114: 268–278.
11. Yokomizo T, Dzierzak E (2010) Three-dimensional cartography of hematopoietic clusters in the vasculature of whole mouse embryos. Development 137: 3651–3661.
12. Kumano K, Chiba S, Kunisato A, Sata M, Saito T, et al. (2003) Notch1 but not Notch2 is essential for generating hematopoietic stem cells from endothelial cells. Immunity 18: 699–711.
13. Yoder MC, Hiatt K, Dutt P, Mukherjee P, Bodine DM, et al. (1997) Characterization of definitive lymphohematopoietic stem cells in the day 9 murine yolk sac. Immunity 7: 335–344.
14. Garcia-Porrero JA, Godin IE, Dieterlen-Lievre F (1995) Potential intraembryonic hemogenic sites at pre-liver stages in the mouse. Anat Embryol (Berl) 192: 425–435.
15. Garcia-Porrero JA, Manaia A, Jimeno J, Lasky LL, Dieterlen-Lievre F, et al. (1998) Antigenic profiles of endothelial and hemopoietic lineages in murine intraembryonic hemogenic sites. Dev Comp Immunol 22: 303–319.
16. Fraser ST, Ogawa M, Yokomizo T, Ito Y, Nishikawa S (2003) Putative intermediate precursor between hematogenic endothelial cells and blood cells in the developing embryo. Dev Growth Differ 45: 63–75.
17. Jaffredo T, Gautier R, Eichmann A, Dieterlen-Lievre F (1998) Intraaortic hemopoietic cells are derived from endothelial cells during ontogeny. Development 125: 4575–4583.
18. Sugiyama D, Ogawa M, Hirose I, Jaffredo T, Arai K, et al. (2003) Erythropoiesis from acetyl LDL incorporating endothelial cells at the preliver stage. Blood 101: 4733–4738.
19. Sugiyama D, Arai K, Tsuji K (2005) Definitive hematopoiesis from acetyl LDL incorporating endothelial cells in the mouse embryo. Stem Cells Dev 14: 687–696.
20. Bertrand JY, Giroux S, Golub R, Klaine M, Jalil A, et al. (2005) Characterization of purified intraembryonic hematopoietic stem cells as a tool to define their site of origin. Proc Natl Acad Sci U S A 102: 134–139.
21. Zovein AC, Hofmann JJ, Lynch M, French WJ, Turlo KA, et al. (2008) Fate tracing reveals the endothelial origin of hematopoietic stem cells. Cell Stem Cell 3: 625–636.
22. Chen MJ, Yokomizo T, Zeigler BM, Dzierzak E, Speck NA (2009) Runx1 is required for the endothelial to haematopoietic cell transition but not thereafter. Nature 457: 887–891.
23. Bertrand JY, Chi NC, Santoso B, Teng S, Stainier DY, et al. (2010) Haematopoietic stem cells derive directly from aortic endothelium during development. Nature 464: 108–111.
24. Kissa K, Herbomel P (2010) Blood stem cells emerge from aortic endothelium by a novel type of cell transition. Nature 464: 112–115.
25. Boisset JC, van Cappellen W, Andrieu-Soler C, Galjart N, Dzierzak E, et al. (2010) In vivo imaging of haematopoietic cells emerging from the mouse aortic endothelium. Nature 464: 116–120.
26. Sasaki T, Mizuochi C, Horio Y, Nakao K, Akashi K, et al. (2010) Regulation of hematopoietic cell clusters in the placental niche through SCF/Kit signaling in embryonic mouse. Development 137: 3941–3952.
27. Mucenski ML, McLain K, Kier AB, Swerdlow SH, Schreiner CM, et al. (1991) A functional c-myb gene is required for normal murine fetal hepatic hematopoiesis. Cell 65: 677–689.
28. Okuda T, van Deursen J, Hiebert SW, Grosveld G, Downing JR (1996) AML1, the target of multiple chromosomal translocations in human leukemia, is essential for normal fetal liver hematopoiesis. Cell 84: 321–330.
29. Wang Q, Stacy T, Binder M, Marin-Padilla M, Sharpe AH, et al. (1996) Disruption of the Cbfa2 gene causes necrosis and hemorrhaging in the central nervous system and blocks definitive hematopoiesis. Proc Natl Acad Sci U S A 93: 3444–3449.
30. North T, Gu TL, Stacy T, Wang Q, Howard L, et al. (1999) Cbfa2 is required for the formation of intra-aortic hematopoietic clusters. Development 126: 2563–2575.
31. Yuasa H, Oike Y, Iwama A, Nishikata I, Sugiyama D, et al. (2005) Oncogenic transcription factor Evi1 regulates hematopoietic stem cell proliferation through GATA-2 expression. EMBO J 24: 1976–1987.
32. Goyama S, Yamamoto G, Shimabe M, Sato T, Ichikawa M, et al. (2008) Evi-1 is a critical regulator for hematopoietic stem cells and transformed leukemic cells. Cell Stem Cell 3: 207–220.
33. Wood HB, May G, Healy L, Enver T, Morris-Kay GM (1997) CD34 expression patterns during early mouse development are related to modes of blood vessel formation and reveal additional sites of hematopoiesis. Blood 90: 2300–2311.
34. Takakura N, Huang XL, Naruse T, Hamaguchi I, Dumont DJ, et al. (1998) Critical role of the TIE2 endothelial cell receptor in the development of definitive hematopoiesis. Immunity 9: 677–686.
35. Theiler K (1972) The house mouse: development and normal stages from fertilization to 4 weeks of age. Springer, Berlin Heidelberg New York.
36. Kishihara K, Penninger J, Wallace VA, Kundig TM, Kawai K, et al. (1993) Normal B lymphocyte development but impaired T cell maturation in CD45-exon6 protein tyrosine phosphatase-deficient mice. Cell 74: 143–156.
37. Byth KF, Conroy LA, Howlett S, Smith AJ, May J, et al. (1996) CD45-null transgenic mice reveal a positive regulatory role for CD45 in early thymocyte development, in the selection of CD4+CD8+ thymocytes, and B cell maturation. J Exp Med 183: 1707–1718.
38. Mee PJ, Turner M, Basson MA, Costello PS, Zamoyska R, et al. (1999) Greatly reduced efficiency of both positive and negative selection of thymocytes in CD45 tyrosine phosphatase-deficient mice. Eur J Immunol 29: 2923–2933.
39. North TE, de Bruijn MF, Stacy T, Talebian L, Lind E, et al. (2002) Runx1 expression marks long-term repopulating hematopoietic stem cells in the midgestation mouse embryo. Immunity 16: 661–672.
40. Matsubara A, Iwama A, Yamazaki S, Furuta C, Hirasawa R, et al. (2005) Endomucin, a CD34-like sialomucin, marks hematopoietic stem cells throughout development. J Exp Med 202: 1483–1492.
41. O'Rahilly R, Muller F (1987) Development Stages in Human Embryos. Washington: Carnegie Institution of Washington.
42. Tavian M, Peault B (2005) The changing cellular environments of hematopoiesis in human development in utero. Exp Hematol 33: 1062–1069.

Regular Article

HEMATOPOIESIS AND STEM CELLS

Polymorphic *Sirpa* is the genetic determinant for NOD-based mouse lines to achieve efficient human cell engraftment

Takuji Yamauchi,[1] Katsuto Takenaka,[1] Shingo Urata,[1] Takahiro Shima,[1] Yoshikane Kikushige,[1] Takahito Tokuyama,[1] Chika Iwamoto,[1] Mariko Nishihara,[1] Hiromi Iwasaki,[2] Toshihiro Miyamoto,[1] Nakayuki Honma,[3] Miki Nakao,[4] Takashi Matozaki,[5] and Koichi Akashi[1,2]

[1]Department of Medicine and Biosystemic Science, Kyushu University Graduate School of Medical Sciences, Fukuoka, Japan; [2]Center for Cellular and Molecular Medicine, Kyushu University Hospital, Fukuoka, Japan; [3]Innovative Drug Research Laboratories, Kyowa Hakko Kirin Co Ltd, Tokyo, Japan; [4]Department of Bioscience and Biotechnology, Graduate School of Bioresource and Bioenvironmental Sciences, Kyushu University, Fukuoka, Japan; and [5]Division of Molecular and Cellular Signaling, Department of Biochemistry and Molecular Biology, Kobe University Graduate School of Medicine, Kobe, Japan

Key Points

- NOD-specific *Sirpa* polymorphism is the genetic determinant of highly efficient xenograft activity in NOD-based immunodeficient mouse models.

Current mouse lines efficient for human cell xenotransplantation are backcrossed into NOD mice to introduce its multiple immunodeficient phenotypes. Our positional genetic study has located the NOD-specific polymorphic *Sirpa* as a molecule responsible for its high xenograft efficiency: it recognizes human CD47 and the resultant signaling may cause NOD macrophages not to engulf human grafts. In the present study, we established C57BL/6.*Rag2*^{null}*Il2rg*^{null} mice harboring NOD-*Sirpa* (BRGS). BRGS mice engrafted human hematopoiesis with an efficiency that was equal to or even better than that of the NOD.*Rag1*^{null}*Il2rg*^{null} strain, one of the best xenograft models. Consequently, BRGS mice are free from other NOD-related abnormalities; for example, they have normalized C5 function that enables the evaluation of complement-dependent cytotoxicity of antibodies against human grafts in the humanized mouse model. Our data show that efficient human cell engraftment found in NOD-based models is mounted solely by their polymorphic *Sirpa*. The simplified BRGS line should be very useful in future studies of human stem cell biology. (*Blood*. 2013;121(8):1316-1325)

Introduction

Immunodeficient mice are widely used to reconstitute human hematopoiesis by xenotransplantation of hematopoietic stem cells (HSCs).[1,2] This "humanized" mouse model provides a powerful tool with which to evaluate the biologic properties of human HSCs and progenitors in vivo.[3,4] Such xenotransplantation systems have also been used to study human cancer stem cells.[5-8]

Elimination of the lymphoid system is the first step to achieving reconstitution of human hematopoiesis. To deplete T and B cells, the *scid* mutation in the *Prkdc* gene[9-11] or disruption of the recombination activating gene 1 or 2 (*Rag1* and *Rag2*)[12,13] has been introduced into various mouse strains. In addition, to deplete natural killer (NK) cells or their functions, the IL-2 receptor common γ chain subunit (*Il2rg*)[14-16] or beta-2-microglobulin (*B2m*)[17-19] is disrupted.

However, depletion of lymphoid cells is not sufficient and it has been shown empirically that additional strain-specific factors modulate human hematopoietic engraftment in the xenotransplantation setting. For example, within the SCID strain, the SCID with the NOD background was the gold standard for the xenotransplantation assay based on its high efficiency.[11] In fact, recent studies have shown that among the lymphoid-depleted mouse strains, the NOD-*scid* *Il2rg*^{null} (NSG/NOG)[14,15] and NOD.*Rag1*^{null}*Il2rg*^{null} (NOD-RG)[20] strains are the most efficient; the BALB/c.*Rag2*^{null}*Il2rg*^{null} (BALB-RG) strain is the next efficient[21,22]; and the C57BL/6 strains with *scid*,[23] *Rag2*^{null}, *Rag2*^{null}*B2m*^{null}, *Rag2*^{null}*Prf*^{null},[24] or *Rag2*^{null}*Jak3*^{null}[25] mutations are unable to reconstitute human hematopoiesis. The NOD strain has multiple immune deficiencies, including defects of appropriate regulation of the T-lymphocyte repertoire, antigen presenting cell function, NK cell function,[26] and hemolytic complement (C5) and cytokine production from macrophages,[27] and these abnormalities are presumed to collaborate to cause the development of autoimmune diabetes and hemolytic anemia.[26,28] To establish xenotransplantation models, lymphoid-depleted strains have been backcrossed into the NOD/ShiLt–inbred strain multiple times to introduce such numerous NOD-specific abnormalities.[14,15] However, it was unknown whether we could select a genetic determinant(s) specially required to achieve the NOD-specific high engraftment capability for human cells.

Previously, we used positional genetics to characterize the molecular basis for this capability in the NOD strain by measuring the ability of mouse BM stromal layers to support hematopoietic long-term culture-initiating cell activity (LTC-IC) in vitro and identified the strain differences as the polymorphism of the *Sirpa* gene located within the insulin-dependent diabetes (*Idd-13*) locus.[24]

Submitted June 28, 2012; accepted December 9, 2012. Prepublished online as *lood* First Edition paper, January 4, 2013; DOI 10.1182/blood-2012-06-440354.

The online version of this article contains a data supplement.

The publication costs of this article were defrayed in part by page charge payment. Therefore, and solely to indicate this fact, this article is hereby marked "advertisement" in accordance with 18 USC section 1734.

Stroma cells from the NOD BM supports LTC-IC of human cells, but those from C57BL/6 could not. Enforced expression of the NOD-type SIRPA enabled C57BL/6 stroma cells to support human LTC-IC.[24] This in vitro finding is also applicable to the in vivo setting, as shown by another study in which a human *SIRPA* BAC transgene introduced into *Rag2*^{null}*Il2rg*^{null} mice on a mixed 129; BALB/c background significantly improved the efficiency of human hematopoietic engraftment.[29]

SIRPA is a transmembrane protein that contains 3 Ig-like domains within the extracellular region. It is expressed in macrophages, myeloid cells, and neurons, and interacts with its ligand CD47 through its respective IgV-like domains, where the NOD strain has specific polymorphism. CD47 is a member of the Ig superfamily that is ubiquitously expressed in hematopoietic and nonhematopoietic cells. The cytoplasmic region of SIRPA has immunoreceptor tyrosine–based inhibitory motifs, and binding cell-surface CD47 with SIRPA on macrophages provokes inhibitory signals through phosphorylation of these inhibitory motifs of SIRPA,[30] preventing their phagocytic activity.[31-33] A recent study also showed that transgenic expression of mouse CD47 into CD34$^+$CD38$^-$ human fetal liver cells significantly enhanced the human cell engraftment into BALB-RG mice.[34] Based on these data, the binding of NOD-SIRPA with human CD47 might produce signals for mouse macrophages not to engulf human HSCs, which presumably makes the strain permissive for human HSC engraftment.[24]

The most important question was whether the NOD-specific highly efficient human cell engraftment in vivo could be explained solely by the NOD-*Sirpa* polymorphism. In the present study, we established a C57BL/6.*Rag2*^{null}*Il2rg*^{null} (C57BL/6-RG) mouse line harboring the NOD-type *Sirpa*. Our data show clearly that replacement of the C57BL/6-type *Sirpa* with the NOD-type *Sirpa* is sufficient for the C57BL/6-RG strain to be endowed with the xenotransplantation capability that is at least equal to NOD-RG mice. Therefore, we successfully segregated the genetic abnormality responsible for efficient human cell engraftment from multiple genetic abnormalities in the NOD strain. The simplified humanized mouse system established by the new C57BL/6.*Rag2*^{null}*Il2rg*^{null}NOD-*Sirpa* (BRGS) strain should be very useful in improving xenotransplantation strategies in future studies of human cell biology.

Methods

Mice

C57BL/6, C57BL/6.NOD-*Idd13*, NOD, NOD.CB17-*Prkdc*^{scid} (NOD-*scid*), and NOD.Cg-*Rag1*^{tm1Mom}*Il2rg*^{tm1Wjl}/Sz (NOD-RG) mice were purchased from the Jackson Laboratory; C57BL/6.*Rag2*^{tm1Fwa}*Il2rg*^{tm1Wjl} (C57BL/6-RG) mice were purchased from Taconic. All mice were bred and maintained in individual ventilated cages at the Kyushu University Animal Facility and fed with autoclaved food and water. BRGS mice were generated by breeding C57BL/6-RG and C57BL/6.NOD-*Idd13* mice and backcrossed with C57BL/6-RG mice. *Rag2* gene and *Sirpa* gene are located on chromosome 2 with 17.1 cM. First, we repeated the breeding of C57BL/6-RG and C57BL/6.NOD-*Idd13* mice, and after 10 breedings, we obtained the recombination between the *Rag2*$^-$ and the *Sirpa*^{NOD} loci by chromosomal crossover. This was examined by genotyping by the microsatellite markers *D2Mit447* and *D2Mit338*, which are 0.63 cM apart on chromosome 2, during interbreeding. In addition, *Sirpa, Rag2*, and *Il2rg* were genetically typed by PCR and direct sequencing. In C57BL/6.NOD-(*D2Mit447-D2Mit338*) *Rag2*^{null}*Il2rg*^{null} mice, the region between *D2Mit447* and *D2Mit338* contains 33 genes, including *Sirpa*, but *Sirpa* is the only gene within the *Idd13* locus that is expressed in BM stromal cells and macrophages and had coding sequence polymorphism between the NOD and other strains.[24] Therefore, we refer to our established mouse line as BRGS herein. Sequences of the oligonucleotide primers used are provided in supplemental Table 1 (available on the *Blood* Web site; see the Supplemental Materials link at the top of the online article). All experiments were conducted following the guidelines of the institutional animal committee of Kyushu University.

Binding affinity of mouse macrophages to human CD47-Fc

Mouse macrophages were obtained by peritoneal lavage. Cells were stained with purified anti–mouse Sirpa (P84; BD Biosciences) conjugated with PE and anti–mouse CD11b (3A33; Beckman Coulter) conjugated with FITC. CD11b$^+$SIRPA$^+$ cells were defined as mature macrophages. The binding between SIRPA and CD47 was assessed by staining with biotinylated human CD47-Fc conjugated with streptavidin-allophycocyanin (APC),[35] and analyzed with a FACSAria III cell sorter (BD Biosciences).

In vitro mouse macrophage phagocytosis assays for human hematopoietic stem cells

Phagocytic activity of mouse macrophages against the human CD34$^+$CD38$^-$ population that contains the majority of human HSCs was evaluated in vitro, as described previously.[36] In brief, mouse peritoneal-derived macrophages were incubated at 1.0×10^4 cells in 200 μL of RPMI 1640 medium in Falcon culture tubes (2058; BD Biosciences). Cells were opsonized with CD34 antibody (sc-19621; Santa Cruz Biotechnology), incubated with mouse IFN-γ (100 ng/mL; R&D Systems) for 24 hours, and then lipopolysaccharide (0.3 μg/μL) for 1 hour. Human cord blood (CB) HSCs were then added to the tubes. Two hours after coincubation with macrophages and target cells, the phagocytic index was calculated using the following formula: phagocytic index = number of ingested cells/(number of macrophages/100). At least 200 macrophages were counted by a blinded observer.

Sensitivity of BRGS mice to irradiation

Cohorts of BRGS mice were exposed to varying doses of the whole-body irradiation from a ^{137}Cs γ-irradiator. The mice were examined daily and euthanized when moribund. Surviving mice were euthanized at 8 weeks after irradiation. NOG/NSG mice are highly radiosensitive because of the *scid* mutation. To examine the radiosensitivity of BRGS mice, 6- to 10-week-old BRGS mice were irradiated with 550-670 cGy, and monitored for 8 weeks. Early deaths were observed in the mouse group irradiated with more than 620 cGy, whereas those irradiated with 550-580 cGy survived at the end of 8 weeks. Based on these data, we irradiated BRGS mice at 580 cGy in all xenotransplantation experiments. The irradiation doses for experiments with NOD-RG (420 cGy) and C57BL/6-RG (670 cGy) were decided by radiosensitivity experiments.

Transplantation of human HSCs into mice

CB cells were collected during normal full-term deliveries after obtaining informed consent in accordance with the Declaration of Helsinki (provided by the Kyushu Block Red Cross Blood Center, Japan Red Cross Society). Mononuclear cells were separated by Ficoll-Hypaque density-gradient centrifugation. Lineage-depleted CB cells were obtained magnetically using a lineage cell depletion kit (Miltenyi Biotec). A total of 5×10^3 CD34$^+$CD38$^-$ cells were injected intrafemorally into mice. Within an individual experiment, mice of each strain received CD34$^+$CD38$^-$ cells purified from the same mixture of CB cells from multiple donors. After transplantation, mice were given sterile water containing prophylactic enrofloxacin (Baytril; Bayer HealthCare). Mice were killed 8, 16, or 24 weeks after transplantation.

Antibodies, cell staining, and sorting

For the analyses of mouse T, B, and NK cells, mouse peripheral blood cells were stained with PE-conjugated anti-CD3 (145-2C11), FITC-conjugated

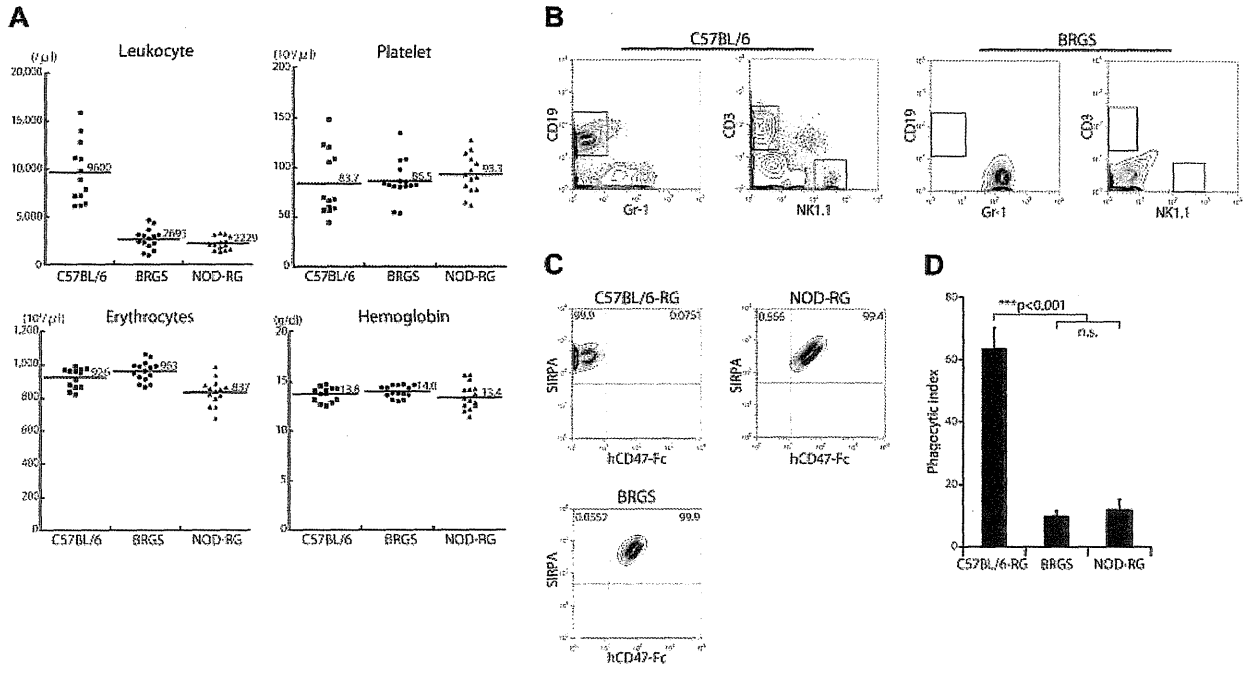

Figure 1. BRGS mice lack lymphocytes and SIRPA recognizes human CD47-Fc. (A) Frequencies of blood leukocytes, erythrocytes, hemoglobin, and platelets in BRGS mice. Leukocyte counts in BRGS ($2.69 \pm 1.01 \times 10^3/\mu L$) and NOD-RG mice ($2.23 \pm 0.7 \times 10^3/\mu L$) are significantly decreased compared with that in C57BL/6 mice ($9.6 \pm 0.32 \times 10^3/\mu L$). BRGS mice have normal erythrocyte ($9.63 \pm 0.63 \times 10^6/\mu L$), hemoglobin ($14.0 \pm 0.6$ g/dL), and platelet ($8.7 \pm 2.0 \times 10^5/\mu L$) counts. (B) Representative FACS plots of blood in C57BL/6 and BRGS mice. BRGS mice lacked T, B, and NK cells. (C) Binding activity of human CD47-Fc to SIRPA expressed in peritoneal macrophages derived from C57BL/6-RG, BRGS, or NOD-RG mice. Macrophages from BRGS and NOD-RG mice, but not those from C57BL/6-RG mice, were stained with human CD47-Fc on FACS. (D) Phagocytosis assay of C57BL/6-RG, BRGS, or NOD-RG macrophages against human $CD34^+CD38^-$ CB HSCs (n = 3). The phagocytic index was determined as the number of engulfed cells per 100 macrophages. Bars indicate mean ± SD.

anti-CD19 (1D3), APC-conjugated anti-NK1.1 (PK136; BD Biosciences), and Pacific Blue–conjugated anti–Gr-1 (RB6-8C5; BioLegend). Sorting of $CD34^+CD38^-$ subfractions was accomplished by staining lineage-depleted CB cells with FITC-conjugated anti-CD34 (581/CD34) and PE-conjugated anti-CD38 (HIT2; BD Biosciences). For analysis and sorting of human cells in the immunodeficient mice, FITC-conjugated anti-CD4 (RPA-T4), CD33 (HIM3-4), CD41a (HIP8), TCR αβ (WT31), TCR γδ (11F2), Igλ L chain (JDC-12), Igκ L chain (G20-193; BD Biosciences), anti-CD10 (SS2/36; Dako), PE-conjugated anti-CD8 (RPA-T8), CD20 (2H7), NKp46 (9E2; BD Biosciences), CD235a (JC159; Dako), PE-Cy7–conjugated anti-CD3 (SK7; BD Biosciences), CD19 (HIB19; BioLegend), APC-conjugated anti-CD45 (J33; Beckman Coulter), and PaB-conjugated anti–mouse CD45 (30-F11; BioLegend) monoclonal antibodies were used in addition to the antibodies described in the preceding paragraph. Nonviable cells were excluded by propidium iodide staining. The cells were analyzed and sorted with a FACSAria cell sorter (BD Biosciences).

Complement-dependent hemolytic activity

To estimate the serum complement activity of mice, the peripheral blood of mice were collected in 1.5-mL tubes and allowed to stand at room temperature for 1 hour. The serum was collected after centrifugation of the blood at 200*g* for 15 minutes at 4°C and stored −80°C until use. The mixtures of each diluted sera of mice, 3.75×10^6 erythrocytes of sheep and 2.5μg of zymosan (Imgenex) were incubated 10 hours at 37°C. After incubation, the absorbance of each sample at 415 nm was measured.

In vivo antibody treatment in a disseminated lymphoma xenograft model

A total of 8×10^5 Raji cells (Burkitt lymphoma cell line; American Type Culture Collection) were injected into BRGS or NOD-RG mice (6-10 weeks of age) via the tail vein. Raji cells proliferated predominantly in the BM. Ten days after injection, these mice were IP injected daily with 200 μg of rituximab or mouse IgG2a control for 1 week and then BM cells were collected and analyzed with the FACSAria III.

Statistical analysis

Data are presented as means ± SD. The significance of the differences between groups was determined via the Student *t* test. For comparison of complement-dependent hemolytic activity among the mouse strains, repeated-measures ANOVA was performed.

Results

Establishment of the BRGS mouse

The BRGS mouse line was established by breeding the C57BL/6-RG with the C57BL/6.NOD-*Idd13* mouse that is congenic for NOD-derived *Idd13* locus within which the *Sirpa* is the only gene that is polymorphic and is expressed in the BM stromal cells.[24] BRGS mice were all born healthy and displayed good fertility. They showed a median life span of 65 weeks without the development of lymphoma that usually occurs in the NOD-*scid* strain after the age of > 5 months.[11]

As shown in Figure 1A, BRGS mice had normal levels of hemoglobin and platelets, but a low number of leukocytes. This is because of the lack of $CD3^+$ T cells, $CD19^+$ B cells, and $NK1.1^+$ NK cells (Figure 1B). IP macrophages from either C57BL/6-RG, BRGS or NOD-RG mice were evaluated for the binding to human CD47 on FACS. $CD11b^+$ peritoneal macrophages strongly expressed SIRPA in all of these strains. As shown in Figure 1C, both macrophages from the BRGS and those from the NOD-RG strain bound to the human CD47-Fc protein, whereas those from the

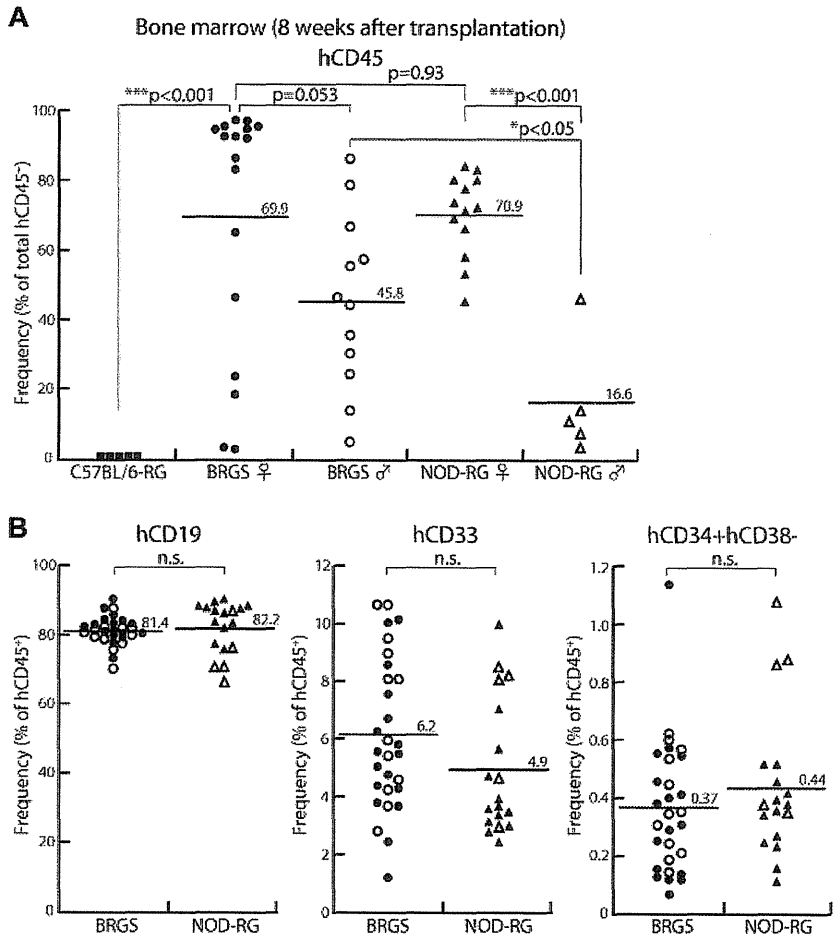

Figure 2. BRGS mice show efficient engraftment of human HSCs comparable to NOD-RG mice. In the BM, human HSC engraftment was examined by flow cytometric analysis 8 weeks after transplantation. C57BL/6-RG mice (■; n = 5), female BRGS mice (●; n = 17), male BRGS mice (○; n = 12), female NOD-RG mice (▲; n = 13), and male NOD-RG mice (△; n = 5) mice were analyzed. (A) Both BRGS and NOD-RG female mice showed excellent human CD45$^+$ reconstitution. BRGS male mice showed significantly better engraftment compared with NOD-RG male mice. (B) Frequencies of CD19$^+$ B cells, CD33$^+$ myeloid cells, and CD34$^+$CD38$^-$ HSCs in BRGS and NOD-RG mice.

C57BL/6 strain did not, confirming that BRGS mice have the NOD-type SIRPA that can bind to human CD47. Consistent with these binding data, when macrophages of each strain were cultured with human CD34$^+$CD38$^-$ cells, macrophages from C57BL/6-RG mice, but not those from BRGS or NOD-RG mice, actively engulfed human CD34$^+$CD38$^-$ cells, as shown by the significant elevation of the phagocytic index in the C57BL/6-RG mice (Figure 1D).

BRGS mice are capable of multilineage reconstitution of human hematopoiesis with efficiency at least equal to that of NOD-RG mice

A recent study has shown that intrafemoral injection is more efficient than IV injection in the xenotransplantation setting.[37] We used intrafemoral injection into adult mice in the present study because our preliminary data also showed that human cell chimerisms of adult BRGS by intrafemoral injection was significantly better than those with IV injection (data not shown). We transplanted 5 × 10^3 CD34$^+$CD38$^-$ human CB cells intrafemorally into C57BL/6-RG, BRGS or NOD-RG mice at the age of 6-8 weeks. Before transplantation, C57BL/6-RG, BRGS, and NOD-RG mice were irradiated with 670, 580, and 420 cGy, respectively. Each dose was set by irradiation tolerance experiments (see the Methods).

At 8 weeks after transplantation, human CD45$^+$ cells were not detectable in C57BL/6-RG mice (Figure 2A). Both BRGS and NOD-RG showed successful reconstitution and their average frequencies of human CD45$^+$ cells were 59.9% and 55.8%, respectively. Recent studies have shown that in the NSG strain,[15] female recipients better support the reconstitution of human hematopoiesis, although the underlying mechanism for this remains unclear.[38,39] As shown in Figure 2A, NOD-RG and BRGS female mice showed equally excellent human CD45$^+$ reconstitution at approximately 70% chimerism. NOD-RG male mice, however, showed significantly poor reconstitution (16.6% of human cell chimerism on average) compared with NOD-RG female mice. In contrast, the percentages of human cell chimerisms in BRGS male mice (approximately 45%) were only slightly lower than those in BRGS female mice and, as a result, BRGS male mice showed significantly better engraftment compared with NOD-RG male mice.

In the BM, the percentages of CD19$^+$ B cells, CD33$^+$ myeloid cells, and CD34$^+$CD38$^-$ cells that contain the majority of human HSCs were almost equal between the BRGS and the NOD-RG strains irrespective of sex (Figure 2B). Representative FACS plots at 8 weeks after injection are shown in Figure 3A. In the spleen, small numbers of CD3$^+$ T cells and CD3$^-$NKp46$^+$ NK cells, as well as CD41$^+$ megakaryocytes and CD235a$^+$ erythrocytes, were found in both BRGS and NOD-RG mice (Figure 3A) and there was no significant difference in the percentages of these cells between the 2 strains regardless of sex. The majority of human cells in the spleen were CD19$^+$ B cells (Figure 3B). Although BM human